



Compressive sensing reconstruction of 3D wet refractivity based on GNSS and InSAR observations

Marion Heublein¹ · Fadwa Alshawaf² · Bastian Erdnüß¹ · Xiao Xiang Zhu³ · Stefan Hinz¹

Received: 8 December 2017 / Accepted: 11 May 2018
© The Author(s) 2018

Abstract

In this work, the reconstruction quality of an approach for neutrospheric water vapor tomography based on Slant Wet Delays (*SWDs*) obtained from Global Navigation Satellite Systems (GNSS) and Interferometric Synthetic Aperture Radar (InSAR) is investigated. The novelties of this approach are (1) the use of both absolute GNSS and absolute InSAR *SWDs* for tomography and (2) the solution of the tomographic system by means of compressive sensing (CS). The tomographic reconstruction is performed based on (i) a synthetic *SWD* dataset generated using wet refractivity information from the Weather Research and Forecasting (WRF) model and (ii) a real dataset using GNSS and InSAR *SWDs*. Thus, the validation of the achieved results focuses (i) on a comparison of the refractivity estimates with the input WRF refractivities and (ii) on radiosonde profiles. In case of the synthetic dataset, the results show that the CS approach yields a more accurate and more precise solution than least squares (LSQ). In addition, the benefit of adding synthetic InSAR *SWDs* into the tomographic system is analyzed. When applying CS, adding synthetic InSAR *SWDs* into the tomographic system improves the solution both in magnitude and in scattering. When solving the tomographic system by means of LSQ, no clear behavior is observed. In case of the real dataset, the estimated refractivities of both methodologies show a consistent behavior although the LSQ and CS solution strategies differ.

Keywords Global navigation satellite system (GNSS) · GNSS tomography · SAR interferometry (InSAR) · Water vapor tomography · Compressive sensing · Least squares

1 Introduction

An accurate knowledge of the three-dimensional (3D) distribution of water vapor in the atmosphere is a key element for weather forecasting and atmospheric modeling. Also, a precise determination of water vapor is required for accurate positioning and deformation monitoring using Global Navigation Satellite Systems (GNSS) and Interferometric Synthetic Aperture Radar (InSAR). The water vapor content

is highly variable both in horizontal and vertical directions, particularly in the lowest atmospheric layers. Several approaches for 3D tomographic water vapor reconstruction from GNSS-based slant wet delay (*SWD*) estimates using the least squares (LSQ) adjustment were presented in the previous years, e.g., in Benevides et al. (2016), Champollion et al. (2004), Chen and Liu (2016), Flores et al. (2000), Hirahara (2000), Notarpietro et al. (2008), Song et al. (2006), Troller et al. (2006), Xia et al. (2013), Yao and Zhao (2016), and Yao and Zhao (2017).

Thanks to the launch of modern SAR missions such as Envisat, TerraSAR, CosmoSkymed, or Sentinel-1, activities of Persistent Scatterer Interferometry (PSI) processing increased a lot. During PSI processing, atmospheric phase screen (APS) can be estimated over wide areas (Hanssen 2001; Parker 2017; Tang et al. 2016) at a relatively high temporal sampling of six days. Therefore, InSAR became a valuable resource for water vapor research.

The main challenges for tomographic approaches consist in the limited number of rays in different ray directions and

✉ Marion Heublein
marion.heublein@kit.edu

¹ Karlsruhe Institute of Technology, Institute of Photogrammetry and Remote Sensing, 76128 Karlsruhe, Germany

² German Research Centre for Geosciences, Telegrafenberg A17, 14473 Potsdam, Germany

³ German Aerospace Center (DLR), Remote Sensing Technology Institute (IMF) and Technical University of Munich (TUM), Signal Processing in Earth observation, Arcisstr. 21, 80333 Munich, Germany

in the ill-posed nature of the inverse problem. Yet, the ray geometry is fix. Even when using observations from different GNSS and from several consecutive epochs, some parts of the atmosphere will not be crossed by any rays. The ill-conditioning is commonly overcome by adding constraints and prior information. However, the constraints often impose an unnatural behavior to the refractivity estimate, and the solution is not adaptive to the real water vapor distribution anymore.

In this work, absolute InSAR *SWDs* are introduced as additional observations and a new constraint for the stabilization of the tomographic system is proposed. The presented compressing sensing (CS) approach benefits of the sparsity of the solution as prior for regularization. A signal is called *sparse*, if it contains only a few nonzero coefficients and many coefficients equal or very close to zero. Yet, in water vapor tomography approaches, the 3D refractivity signal is not sparse at all. Therefore, the CS estimation is performed in a transform domain, in which the refractivity signal can be sparsely represented. The main motivation for using CS instead of a classical least squares approach lies in the capacity of CS to recover sparse signals using only a small number of measurements. In addition, when using CS, there is no need anymore for the explicitly defined geometric constraints applied in many previous tomography studies.

The main contributions of this paper are

- the use of absolute GNSS and InSAR *SWDs* for water vapor tomography and
- the introduction of a compressive sensing solution for the tomographic equation.

2 Related work

The current methodologies for tomographic water vapor reconstruction based on GNSS *SWD* estimates can be distinguished into iterative and non-iterative techniques. The work in Bender et al. (2011) analyzes different algebraic reconstruction techniques (ART) that iteratively process observation by observation without performing any matrix inversion. In contrast, Champollion et al. (2004), Flores et al. (2000), Hirahara (2000), Notarpietro et al. (2008), Rohm (2013), Song et al. (2006), and Troller et al. (2006) apply non-iterative approaches solving the inverse system by means of singular value decomposition (SVD). Alternatively, Gradinarsky and Jarlemark (2004) propose a Kalman filter approach. A combination of iterative and non-iterative techniques is presented by Xia et al. (2013). They firstly use iterative reconstruction algorithms in order to determine a refractivity field that they then use as initial values for a non-iterative tomography approach.

For both iterative and non-iterative reconstruction methodologies, the regularization of the ill-conditioned tomographic systems for neutrospheric water vapor reconstruction can be achieved i) by adding constraint equations, which can be considered as pseudo-observations, ii) by adding additional data from other sensors, models, or simulations, or iii) by increasing the number of voxels crossed by rays. The number of voxels crossed by rays can be increased, e.g., by adapting the voxel sizes to the ray density, or by including rays entering the study area both on its top and on its side, instead of only using rays entering the volume on its top. In addition, when considering a general inverse approach based on singular value decomposition, the inverse system can be stabilized by carefully selecting the meaningful singular values.

Both Flores et al. (2000) and Gradinarsky and Jarlemark (2004) apply horizontal and vertical smoothing constraints as well as a boundary constraint assuming zero refractivity above a certain height. In Song et al. (2006), the horizontal smoothing constraints are implemented by assuming a certain degree of correlation between neighboring voxels using Gaussian weighted mean with controllable width. The authors of Gradinarsky and Jarlemark (2004) state that this Gaussian weighted mean can also be applied to the vertical direction. Alternatively, an exponential refractivity decay with increasing height can be assumed, as proposed in Elosegui et al. (1998). The work in Heublein et al. (2015) uses the sparsity of the signal in a specific, predefined transform domain as a prior for regularization and then reconstructs the signal by means of L_1 norm minimization. While helping a lot in regularizing the solution, both geometric constraints and exponential decay in most cases do not reflect the real atmospheric state.

In addition to the constraints, prior knowledge can be added as pseudo-observations to the ill-posed system of equations. The authors of Flores et al. (2000) add radiosonde profiles, and Champollion et al. (2005) state that instead of radiosonde profiles, a standard atmosphere could be used as a priori field. Moreover, Champollion et al. (2005) and Xia et al. (2013) propose the use of water vapor profiles above 2 km from radio occultation, e.g., from the Constellation Observing System for Meteorology, Ionosphere and Climate (COSMIC). In addition, Champollion et al. (2005) propose the use of surface meteorological observations in order to gain stability in the lowest layer. Besides, Song et al. (2006) use a priori knowledge from numerical weather prediction. According to Chen and Liu (2016), data from water vapor radiometers and sun photometers can also be introduced into the tomographic system. In order to minimize smoothing effects of geometrical constraints, Benevides et al. (2016) introduce maps of temporal changes of precipitable water vapor provided by InSAR as a constraint to GNSS tomography.

The studies in Yao and Zhao (2016) and Yao and Zhao (2017) suggest a tomography approach which helps to further reduce the number of voxels without crossing signals. In Yao and Zhao (2016), first of all, they increase the utilization rate of *SWD* observations by selecting a reasonable vertical tomography boundary based on several years of radiosonde observations. Then, they propose a two-step refractivity estimation in order to optimally use GNSS rays entering the study area both on its top and on its side. They first define a study area larger than the tomographic grid of interest and estimate the refractivities of this study area by only using the rays entering the area on its top. Thereafter, they reduce the study area to the final tomographic grid. Based on the refractivities determined within the larger study area, they are able to introduce a scale factor describing, for each ray, the ratio of *SWD* within or outside of the study area. By means of this scale factor, the total *SWDs* of side rays can be reduced to the portion of *SWDs* corresponding to the tomographic grid, and the reduced side ray *SWDs* can be appended to the observation equation. Although the number of voxels passed by rays of the Global Positioning System (GPS) is increased by the work of Yao and Zhao (2016), horizontal smoothing constraints and vertical a priori conditions are still necessary for the solution of the tomographic system. The work in Yao and Zhao (2017) is based on a non-uniform symmetrical division of horizontal voxels distributing the available information more evenly among all voxels than in the case of regular voxel divisions.

A similar idea of decreasing the number of voxels without crossing rays is pursued by Rohm (2013), introducing a combination of consecutive epochs of data and assuming the availability of at least three interoperable GNSS. Based on the combination of many epochs of observations linked with one state of the atmosphere, Rohm (2013) presents an unconstrained approach for water vapor tomography. The approach relies on a careful selection of meaningful singular values in the process of pseudo-inverse and is applied to a synthetic dataset. Adding *SWD* estimates from other GNSS than GPS to the tomographic system increases the number of crossed voxels. However, as there are only rays traveling from satellites in space to receivers on ground, the ray geometry remains limited and there still remain voxels that are not crossed by any rays at all. That is, the tomographic system is still under-determined and needs to be regularized by constraints, or, as proposed by Rohm (2013), by carefully selecting the singular values used for the solution of the inverse system.

Introducing InSAR *SWD* differences into the tomographic system as proposed by Benevides et al. (2016) reduces the smoothing effects observed when using horizontal constraints for the regularization of the tomographic system. However, Benevides et al. (2016) consider temporal changes of precipitable water (*PW*) only. Moreover, they

do not carefully distinguish the different components composing the precipitable water. As shown in Alshawaf et al. (2015b), the *PW* is composed of a stratified (elevation-dependent) component, a turbulently mixed short-scale component, as well as a long-wavelength component. If InSAR atmospheric phases are transformed into *PW* maps as shown in Benevides et al. (2016), due to InSAR processing, parts of the elevation-dependent component as well as the long-wavelength *PW* may be missing. These drawbacks of InSAR processing for water vapor analyses are overcome in the work of Alshawaf et al. (2015b), presenting a method to combine *PW* estimated at GNSS sites and *PW*-difference maps extracted from InSAR interferograms to produce maps of absolute *PW* at high spatial resolution. In addition, in Alshawaf et al. (2015a), a data fusion of InSAR, GNSS, and simulations of the Weather Research and Forecasting (WRF) model is applied to produce *PW* maps.

In this work, we will explore compressive sensing and sparse reconstruction for 3D tomographic water vapor reconstruction. As sparse signals are commonly expected, pioneer research has been carried out to apply CS for solving various remote sensing problems (Zhu and Bamler 2015). Examples include SAR imaging (Potter et al. 2010; Alonso et al. 2010), optimizing remote sensing systems (Zhang et al. 2012), SAR tomography (Aguilera et al. 2013; Budillon et al. 2011; Zhu and Bamler 2010, 2014), ground moving target identification (GMTI) (Prunete 2010), inverse SAR (ISAR) (Zhang et al. 2010), pan-sharpening and hyperspectral image enhancement (Grohnfeldt et al. 2013; Jiang et al. 2014; Li and Yang 2011; Zhu et al. 2016; Zhu and Bamler 2013), and spectral unmixing for hyperspectral data (Bieniarz et al. 2015; Iordache et al. 2011). For all above-mentioned applications, compared to the classic LSQ (possibly along with L_2 norm regularization), compressive sensing and sparse reconstruction led to exciting results.

3 Characteristics of GNSS and InSAR

Both GNSS and InSAR have an all-weather observing capability. Using the method of Precise Point Positioning (PPP) described in Kouba and Héroux (2001), GNSS yield point-wise estimates of integrated slant wet delays caused by neutrospheric water vapor. Their spatial resolution depends on the density of the observing sites, and each estimated value represents the neutrospheric effect within a cone with vertex at the GNSS site. In contrast to the GNSS horizontal resolution depending on the GNSS inter-site distances, the spatial resolution of InSAR is significantly high, e.g., $5 \text{ m} \times 20 \text{ m}$ in C-band interferometric wide-swath mode (Envisat, Sentinel-1), as indicated in Berger et al. (2012). In PSI, depending on the local PS distribution, even better spatial resolutions can be obtained. The InSAR data processing for this study is based

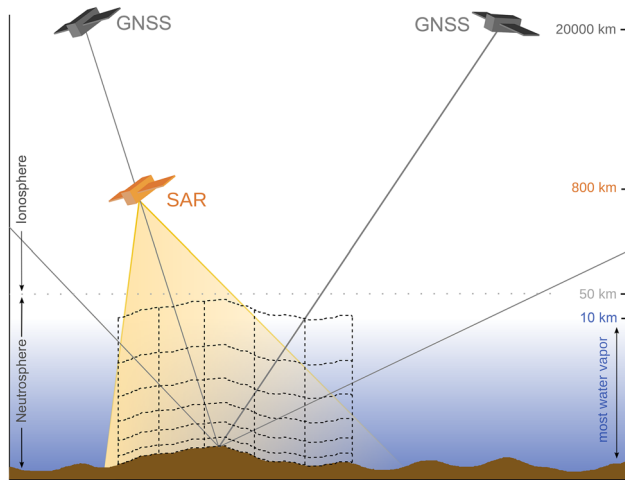


Fig. 1 Observing geometry of GNSS and InSAR. The Envisat satellite following a sun-synchronous orbit observed the Upper Rhine Graben study area 2 (real dataset) at 9h48 UTC under a slightly variable viewing angle. In contrast, both the elevation and azimuth angles of the GNSS satellites observed from study area 2 are not constant over time

on Envisat ASAR observations and is done using the Persistent Scatterer Interferometry introduced by Hooper et al. (2007).

The observing geometry of GNSS and InSAR is illustrated in Fig. 1. In the case of SAR satellites traveling in a near-circular sun-synchronous orbit, the study region is observed from a geometry varying only slightly from acquisition time to acquisition time. The traversed atmospheric section remains almost the same. This is different for GNSS, where the visibility of the satellites at a constant acquisition time varies from day to day. Hence, the GNSS azimuth and elevation angles vary at the different acquisition dates, and the GNSS signal does not travel the same atmospheric section as the InSAR signal.

4 Physical foundations

The total refractivity and the total delay on radio wave signals caused by refractivity are commonly subdivided into two parts, e.g., into a *dry* and a *wet* component or into a *hydrostatic* and a *non-hydrostatic* part. The dry component only contains the delay caused by the dry gases. In contrast, the hydrostatic component also contains contributions of water vapor. If a hydrostatic equilibrium can be assumed, the hydrostatic component can be accurately computed based on surface pressure. Therefore, in this work, the total refractivity or delay is subdivided into a hydrostatic and a non-hydrostatic part. However, for reasons of readability, and consistently with the IERS conventions of Petit and Luzum (2010), the terms *wet* refractivity resp. *wet* delay are used in the fol-

lowing for the non-hydrostatic component of the refractivity resp. of the delay.

Then, according to Bevis et al. (1992), the 3D wet refractivity field N_{wet} (ppm) with (ppm) standing for (mm/km) is related to the partial pressure of water vapor e (hPa) and to the temperature T (K) as follows:

$$N_{\text{wet}} \text{ (ppm)} = k'_2 \cdot \frac{e}{T} + k_3 \cdot \frac{e}{T^2} \quad (1)$$

with

$$k'_2 = k_2 - k_1 \cdot \frac{M_{\text{water vapor}}}{M_{\text{dry air}}} \quad (2)$$

from Davis et al. (1985) and constant factors k_1 , k_2 , and k_3 , e.g., from Smith and Weintraub (1953):

$$\begin{aligned} k_1 &= 77.6 \text{ K/hPa} \\ k_2 &= 72 \text{ K/hPa} \\ k_3 &= 3.75 \times 10^5 \text{ K}^2/\text{hPa} \end{aligned} \quad (3)$$

The variables $M_{\text{water vapor}}$ and $M_{\text{dry air}}$ in Eq. 2 stand for the molar masses of water vapor and dry air.

Alternatively, the 3D water vapor distribution can be expressed by the water vapor mixing ratio

$$w_v \text{ (g/kg)} = \frac{m_{\text{water vapor}}}{m_{\text{dry air}}} \quad (4)$$

or the specific humidity

$$q_v \text{ (g/kg)} = \frac{w_v}{1 + w_v} = \frac{m_{\text{water vapor}}}{m_{\text{total air}}}, \quad (5)$$

which can be related to the 3D wet refractivity field by solving

$$q_v \text{ (g/kg)} = \frac{\epsilon' \cdot e}{p - e(1 - \epsilon')} \quad (6)$$

from Stull (2016) for the partial pressure of water vapor:

$$e \text{ (hPa)} = \frac{q_v \cdot p}{\epsilon' + q_v \cdot (1 - \epsilon')} \quad (7)$$

In Eq. 7, p (hPa) is the atmospheric pressure and $m_{\text{water vapor}}$ (g) and $m_{\text{total air}}$ (kg) are the mass of water vapor within the air and the mass of the total air, respectively. The ratio between the gas constant of dry air and the gas constant of pure water vapor $\epsilon' = 0.622$ is used.

Integrating N_{wet} along the i th slant ray path sp_i with differentials dl yields the observation equation for SWD_i

$$SWD_i \text{ (m)} = 10^{-6} \cdot \int_{sp_i} N_{\text{wet}} \text{ (ppm)} dl \text{ (m)}, \quad (8)$$

or, along discretized segments d_{ij} of the slant ray path,

$$SWD_i \text{ (mm)} = \sum_{j=1}^L N_{\text{wet},j} \text{ (ppm)} \cdot d_{ij} \text{ (km)}, \quad (9)$$

where d_{ij} is the distance passed by the slant ray path i within voxel j , and L is the total number of voxels within some tomographic grid. In addition, the 3D wet refractivity field can be related to further integrated quantities like the Precipitable Water, the Integrated Water Vapor (IWV), or the Zenith Wet Delay (ZWD) as indicated in Fig. 2. The discretized formula for obtaining PW is given in the following equation:

$$PW \text{ (mm)} = \sum_{j=1}^L q_{v_j} \text{ (g/kg)} \cdot \rho \cdot d_{\text{zenith},j} \text{ (km)} \quad (10)$$

where $d_{\text{zenith},j}$ represents the distance passed by the zenith ray path crossing the voxel j , and $\rho = 1 \text{ g/cm}^3$ is the density of water.

The precipitable water is related to the integrated water vapor (IWV^{zenith}) and to the ZWD as follows:

$$PW = \frac{IWV^{\text{zenith}}}{\rho} = \Pi \cdot ZWD \quad (11)$$

According to Schüller (2001), the conversion factor

$$Q = 0.1022 + \frac{1708.08 \text{ (K)}}{T_m} = \frac{1}{\Pi} \quad (12)$$

can be approximated using

$$T_m \approx 70.2 + 0.72 \cdot T_0 \quad (13)$$

for the computation of the neutrospheric mean temperature T_m based on the surface temperature T_0 .

Figure 2 summarizes the relation between GNSS or InSAR integrated wet delays or Precipitable Water and the 3D water vapor mixing ratios simulated by the WRF model.

5 Methodology

The least squares and compressive sensing methodologies are applied to both a synthetic SWD dataset deduced from WRF and a real SWD dataset originating from GNSS and InSAR observations. In Sect. 5.1, the tomographic model is introduced. In the following two subsections, the least squares and the compressive sensing solution strategies are described.

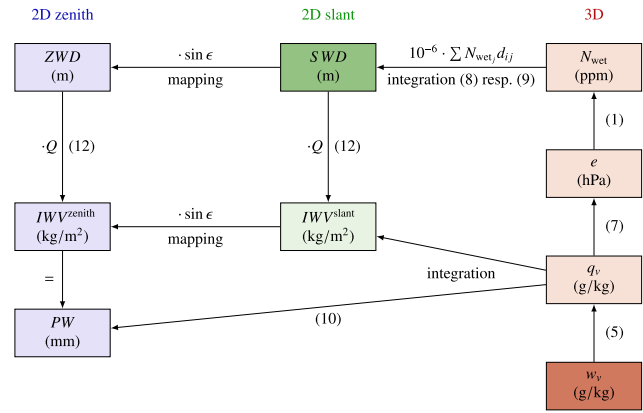


Fig. 2 Meteorological quantities describing the 2D and 3D water vapor distribution in the neutrosphere. The SWD input data for tomography are highlighted in dark green. In case of the synthetic dataset, they are deduced from the WRF water vapor mixing ratios w_v highlighted in dark red. The numbers in the diagram indicate the formula used for the respective steps

5.1 Tomographic model

The work in Flores et al. (2000) introduces the functional model for neutrospheric tomography using GNSS slant wet delays as given in Eq. 8. When aiming at a tomographic reconstruction of the wet refractivity, however, the problem from Eq. 8 is discretized into L volume pixels (voxels) in which the refractivity values, estimated at the voxel centers, are assumed to be constant for this study. These voxels are defined by horizontal and vertical layers of constant geodetic longitude, latitude, and height. The total number of unknown parameters L is defined by the numbers of voxels in longitude P , in latitude Q , and in height K :

$$L = P \cdot Q \cdot K \quad (14)$$

This discretization of the study area into a tomographic grid composed of L voxels is illustrated in Fig. 3.

The raytracing in ellipsoidal coordinate systems is done according to Perler (2011) and the slant wet delay is calculated as in Eq. 9. The raytracing of Perler (2011) allows for three different kinds of intersections between the voxel borders and the ray path. The intersections of a straight ray path with the voxels must be situated (i) at the intersection of the ray path with an unbent plane of constant longitude corresponding to a voxel border in longitude, or (ii) on a cone of constant latitude corresponding to a voxel border in latitude, or (iii) on one of the layers of constant height representing the vertical voxel borders. The intersection points of the first two intersection types are obtained by parameterizing the straight ray, the unbent plane, and the cone mathematically, and by setting equal the expressions (i) for the ray and for the plane resp. (ii) for the ray and for the cone. In case of the third

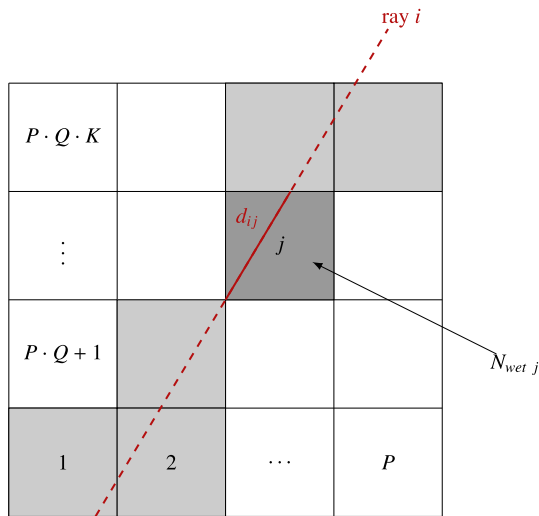


Fig. 3 Schematic illustration of a ray crossing the tomographic voxel grid. Only a vertical 2D slice of the 3D tomographic grid is represented and, schematically, a ray crossing only this 2D slice is shown. The 3D voxel grid would be composed of P voxels in longitude, Q voxels in latitude, and K voxels in height. The black numbers and the variables in the voxel centers represent the voxel numbers. All those voxels that are crossed by ray i are highlighted in light gray. The distance d_{ij} corresponds to the distance that ray i passes within the voxel j highlighted in dark gray

intersection type, a nonlinear system of equations is solved in order to deduce the intersections. This system of equations is obtained by parameterizing constant height layers in ellipsoidal coordinates and by setting these coordinates equal to the parameterization of the straight ray path. For each ray i , d_{ij} corresponds to the distance that the ray passes within a voxel j .

Summarizing all observations SWD_i in an observation vector $\mathbf{y} \in \mathbb{R}^{N \times 1}$ with N being the number of observations, all unknowns $N_{wet,j}$ in a parameter vector $\mathbf{x} \in \mathbb{R}^{L \times 1}$, and all distances d_{ij} in a design matrix $\Phi \in \mathbb{R}^{N \times L}$, the linear system of equations from Eq. 9 can be reformulated in the form

$$\mathbf{y} = \Phi \cdot \mathbf{x}, \tag{15}$$

or, including a weighting matrix $\mathbf{P} \in \mathbb{R}^{N \times N}$ for the observations,

$$\mathbf{P} \cdot \mathbf{y} = \mathbf{P} \cdot \Phi \cdot \mathbf{x}, \tag{16}$$

where

$$\Phi_{i,j} = \begin{cases} d_{ij} & \text{if ray } i \text{ crosses voxel } j \\ 0 & \text{elsewhere.} \end{cases} \tag{17}$$

As each ray only crosses a small subsection of the voxel grid, the matrix Φ contains many zero elements and just a

few nonzero elements. For each row i of the design matrix Φ , the entries Φ_{ij} correspond to the distances d_{ij} that ray i passes within the voxels, as illustrated in Fig. 3. Voxels that are not crossed by any rays yield a zero column in Φ . Only rays entering the study area on its top at 10 km are considered. According to radiosonde measurements, nearly all atmospheric water vapor should reside below this height. Only for the rays entering the study area on its top, the observed SWD can be totally assigned to the voxels within the tomographic grid. If rays entering the study area below its top were considered, the portion of SWD belonging to the study area would have to be estimated, e.g., based on weather models, assuming an exponential humidity decay, or applying a two-step refractivity estimation introducing a scale factor for the water vapor portions within the study area as proposed in Yao and Zhao (2016).

5.2 Classical least squares solution

The term least squares solution already indicates how such a solution is obtained based on a linear functional model as given in Eq. 16. The squares of the observation residuals are minimized:

$$\hat{\mathbf{x}} = \underset{\mathbf{x}}{\operatorname{argmin}} \|\mathbf{P} \cdot \mathbf{y} - \mathbf{P} \cdot \Phi \cdot \mathbf{x}\|_2^2 \tag{18}$$

In the unconstrained Gauß-Markov solution, this is done by means of

$$\hat{\mathbf{x}} = (\Phi^T \cdot \mathbf{P} \cdot \Phi)^{-1} \cdot \Phi^T \cdot \mathbf{P} \cdot \mathbf{y}. \tag{19}$$

Assuming a voxel’s refractivity to equal the mean refractivity of the surrounding voxels within the same height layer, horizontal smoothing constraints can be applied for regularization:

$$N_{wet_{a,b,k}} = \sum_{p,q} w_{p-a,q-b} \cdot N_{wet_{p,q,k}} \tag{20}$$

Here, the voxel indices $p \neq a$ and $q \neq b$ correspond to the remaining voxels in the k th height layer. The refractivity of voxel (a, b) is set to the weighted mean of all but the (a, b) refractivity on the k th height layer. The weights can be, e.g., computed according to inverse distance weighting

$$w_{p-a,q-b} = \begin{cases} \frac{1}{d_{p-a,q-b}} & \text{if } (a, b) \neq (p, q) \\ \frac{1}{\sum_{p,q} \frac{1}{d_{p-a,q-b}}} & \\ -1 & \text{if } (a, b) = (p, q). \end{cases} \tag{21}$$

The distances $d_{p-a,q-b}$ are the distances between the center of voxel (p, q) and the center of voxel (a, b) of the considered height layer.

In addition, according to Davis et al. (1993), an average refractivity profile can be approximated by an exponential decay with height:

$$N_{\text{wet}}(h_k) = N_{\text{wet}}(h_0) \cdot \exp\left(-\frac{h_k - h_0}{H_{\text{scale}}}\right) \quad (22)$$

The height of the k th layer is represented by h_k , h_0 corresponds to some reference height at which the refractivity equals $N_{\text{wet}}(h_0)$, and H_{scale} is the scale height of the local troposphere.

As H_{scale} is a crucial parameter for the definition of an exponential decay with height, its value has been selected during the solution of the tomographic system from a set of realistic values for H_{scale} between 1000 and 2000 m. As detailed below, the selection of H_{scale} is performed in combination with the selection of trade-off parameters weighting the constraints and potential prior knowledge with respect to the *SWD* estimates.

The value of $N_{\text{wet}}(h_0)$ could, e.g., be set to surface refractivities deduced from surface meteorology, or is, in this study, estimated within the adjustment. In order to include $N_{\text{wet}}(h_0)$ into the parameters x , the representation of Eq. 22 is slightly modified. For each $N_{\text{wet}}(h_l)$, $l = 1 \dots L$, Eq. 22 yields one line of a system of equations for the vertical constraint. In matrix notation, with a matrix

$$\tilde{\Phi}_{\text{vert}} = \begin{pmatrix} \exp\left(-\frac{h_0-h_0}{H_{\text{scale}}}\right) & 0 & \dots & 0 \\ \vdots & \vdots & \vdots & \vdots \\ \exp\left(-\frac{h_0-h_L}{H_{\text{scale}}}\right) & 0 & \dots & 0 \end{pmatrix} \quad (23)$$

and a parameter vector

$$x = \begin{pmatrix} N_{\text{wet}}(h_0) \\ \vdots \\ N_{\text{wet}}(h_L) \end{pmatrix}, \quad (24)$$

these lines can be summarized to

$$x = \tilde{\Phi}_{\text{vert}} \cdot x. \quad (25)$$

Consequently, if x is factored out,

$$(\tilde{\Phi}_{\text{vert}} - I) \cdot x = 0 \quad (26)$$

holds, and with

$$\Phi_{\text{vert}} = (\tilde{\Phi}_{\text{vert}} - I), \quad (27)$$

this can be written as

$$\Phi_{\text{vert}} \cdot x = 0. \quad (28)$$

Applying the horizontal and the vertical constraints and introducing prior knowledge from surface meteorology, the observation equation in Eq. 16 can be extended to

$$\begin{pmatrix} P_{\text{data}} \cdot y_{\text{data}} \\ P_{\text{hz}} \cdot y_{\text{hz}} \\ P_{\text{vert}} \cdot y_{\text{vert}} \\ P_{\text{meteo}} \cdot y_{\text{meteo}} \end{pmatrix} = \begin{pmatrix} P_{\text{data}} \cdot \Phi_{\text{data}} \\ P_{\text{hz}} \cdot \Phi_{\text{hz}} \\ P_{\text{vert}} \cdot \Phi_{\text{vert}} \\ P_{\text{meteo}} \cdot \Phi_{\text{meteo}} \end{pmatrix} \cdot x. \quad (29)$$

The matrix $\Phi_{\text{data}} \in \mathbb{R}^{N \times (L+1)}$ is composed of

$$\Phi_{\text{data}} = (0 \quad \Phi) \quad (30)$$

and the constraint matrices $\Phi_{\text{hz}} \in \mathbb{R}^{L \times (L+1)}$

$$\Phi_{\text{hz}} = \begin{pmatrix} 0 & -1 & w_{1,2,1} & \dots & w_{P,Q,1} \\ 0 & w_{2,1,1} & -1 & \dots & \vdots \\ 0 & \vdots & \vdots & \ddots & w_{P,Q,K-1} \\ 0 & w_{1,1,K} & \dots & w_{P,Q,K} & -1 \end{pmatrix} \quad (31)$$

using $w_{a,b,k}$ from Eq. 21 and $\Phi_{\text{vert}} \in \mathbb{R}^{(L+1) \times (L+1)}$ from Eq. 28 are used.

Moreover, additional observations $y_{\text{hz}} \in \mathbb{R}^{L \times 1}$

$$y_{\text{hz}} = 0 \quad (32)$$

and $y_{\text{vert}} \in \mathbb{R}^{(L+1) \times 1}$

$$y_{\text{vert}} = 0 \quad (33)$$

as well as prior knowledge from surface meteorology

$$y_{\text{meteo}} = \Phi_{\text{meteo}} \cdot x \quad (34)$$

are introduced, with $y_{\text{meteo}} \in \mathbb{R}^{(L+1) \times 1}$ and entries of $\Phi_{\text{meteo}} \in \mathbb{R}^{(L+1) \times (L+1)}$

$$\Phi_{\text{meteo } a,b,k} = \begin{cases} 1 & \text{if synoptic site in voxel } (a, b, k) \\ 0 & \text{elsewhere.} \end{cases} \quad (35)$$

No prior knowledge of the surface meteorological site Stuttgart is included.

For equally precise observations, the weighting matrix $P_{\text{data}} \in \mathbb{R}^{N \times N}$ can be set to the identity matrix. Alternatively, P_{data} can, e.g., express a proportionality to the elevation angle of the considered ray path. High elevation observations could be considered to be more precise than observations at low elevation angles. In this study, P_{data} is

set to the identity matrix. Since each constraint shall have a similar impact on all voxels, and since the a priori information from surface meteorology is equally weighted for all voxels in which prior knowledge is available, the entries of $\mathbf{P}_{\text{hz}} \in \mathbb{R}^{N \times N}$, $\mathbf{P}_{\text{vert}} \in \mathbb{R}^{(L+1) \times (L+1)}$, and $\mathbf{P}_{\text{meteo}} \in \mathbb{R}^{(L+1) \times (L+1)}$ only contain the impact of the horizontal and vertical constraints as well as of the prior knowledge from surface meteorology on the data fidelity term. Consequently, Eq. 29 can be reformulated as

$$\begin{pmatrix} \mathbf{I} & \cdot \mathbf{y}_{\text{data}} \\ \mathbf{I} \cdot \lambda_{\text{hz}} & \cdot \mathbf{y}_{\text{hz}} \\ \mathbf{I} \cdot \lambda_{\text{vert}} & \cdot \mathbf{y}_{\text{vert}} \\ \mathbf{I} \cdot \lambda_{\text{meteo}} & \cdot \mathbf{y}_{\text{meteo}} \end{pmatrix} = \begin{pmatrix} \mathbf{I} & \cdot \Phi_{\text{data}} \\ \mathbf{I} \cdot \lambda_{\text{hz}} & \cdot \Phi_{\text{hz}} \\ \mathbf{I} \cdot \lambda_{\text{vert}} & \cdot \Phi_{\text{vert}} \\ \mathbf{I} \cdot \lambda_{\text{meteo}} & \cdot \Phi_{\text{meteo}} \end{pmatrix} \cdot \mathbf{x} \quad (36)$$

with identity matrices \mathbf{I} of appropriate sizes.

Omitting the identity matrices, the LSQ solution to Eq. 29 is then obtained by solving the following minimization problem with the trade-off parameters λ_{hz} , λ_{vert} , and λ_{meteo} for the constraints as well as for the prior knowledge:

$$\hat{\mathbf{x}} = \underset{\mathbf{x}}{\operatorname{argmin}} \left\{ \|\mathbf{y}_{\text{data}} - \Phi_{\text{data}} \cdot \mathbf{x}\|_2^2 + \lambda_{\text{hz}} \cdot \|\mathbf{y}_{\text{hz}} - \Phi_{\text{hz}} \cdot \mathbf{x}\|_2^2 + \lambda_{\text{vert}} \cdot \|\mathbf{y}_{\text{vert}} - \Phi_{\text{vert}} \cdot \mathbf{x}\|_2^2 + \lambda_{\text{meteo}} \cdot \|\mathbf{y}_{\text{meteo}} - \Phi_{\text{meteo}} \cdot \mathbf{x}\|_2^2 \right\}. \quad (37)$$

At the same time as the value of H_{scale} is chosen, the trade-off parameters λ_{vert} , λ_{hz} , and λ_{meteo} are selected from a certain number of logarithmically scaled possible trade-off parameters. This is done in two steps. First, all those combinations of trade-off parameters are preselected that satisfy the eigenvalue cutoff criterion defined in Flores et al. (2000). The work in Hajj et al. (1994) and Wiggins (1972) indicate that the input noise is amplified into the solution by a factor given by the smallest nonzero eigenvalue. Based on $\sigma_y = 5$ mm, and using $\sigma_x = 3.5$ mm/km from Flores et al. (2000), the cutoff value w for the eigenvalues is

$$w = \left(\frac{\sigma_y}{\sigma_x} \right)^2 = 2 \text{ km}^2. \quad (38)$$

This preselection guarantees a large set of stable solutions, which do not necessarily match equally well with the observations. Therefore, in a second step, the combination of trade-off parameters yielding the minimum observation residuals is chosen as final trade-off parameters.

5.3 Proposed compressive sensing solution

If the signal to be reconstructed is sparse, its coefficients only have a small number of nonzeros. In this study, the wet

refractivity signal \mathbf{x} itself is not sparse, but the assumption is that a sparse representation \mathbf{s} of it can be obtained after an appropriate transform $\mathbf{x} = \Psi \cdot \mathbf{s}$. Then, a compressive sensing solution as introduced, e.g., by Baraniuk et al. (2011) and Candès and Wakin (2008), can be applied in order to reconstruct the sparse signal \mathbf{s} in the transform domain.

Instead of estimating the parameters \mathbf{x} in the original domain, the sparse parameters \mathbf{s} are estimated by

$$\hat{\mathbf{s}} = \underset{\mathbf{s}}{\operatorname{argmin}} \left\{ \|\mathbf{y} - \Phi \cdot \Psi \cdot \mathbf{s}\|_2^2 + \lambda_{\text{CS}} \cdot \|\mathbf{s}\|_1 + \lambda_{\text{meteo}} \cdot \|\mathbf{y}_{\text{meteo}} - \Phi_{\text{meteo}} \cdot \Psi \cdot \mathbf{s}\|_2^2 \right\}. \quad (39)$$

That is, instead of adding horizontal and vertical constraints to the data fidelity term as in Eq. 37, an L_1 norm regularization term is introduced to promote sparse solutions for \mathbf{s} . The L_1 norm of \mathbf{s} equals the sum of the coefficients in \mathbf{s} :

$$\|\mathbf{s}\|_1 = \sum_{m=1}^M |s_m| \quad (40)$$

Subsequently, the wet refractivity \mathbf{x} can be reconstructed by

$$\hat{\mathbf{x}} = \Psi \cdot \hat{\mathbf{s}} \quad (41)$$

with a dictionary $\Psi \in \mathbb{R}^{L \times M}$. The dimension M of the parameters $\mathbf{s} \in \mathbb{R}^{M \times 1}$ in the transform domain depends on the number of base functions resp. atoms defined in Ψ . A *base function* resp. *atom* corresponds to one column of Ψ . If Ψ is orthogonal, the terms *transform matrix* and *base function* are commonly used. For more general Ψ that may be rectangular but non-square and therefore not orthogonal at all, the terms *dictionary* and *atom* are preferred. The latter expressions can also be used in a generalizing way for transform matrix and base functions. When referring to languages, an *atom* would correspond to a word within a dictionary. As each word within a language dictionary would be composed of different *letters*, each *atom* within the dictionary for sparse representation is obtained by Kronecker multiplication of smaller items that will be called *letters* in the following.

Considering a tomographic reconstruction of water vapor, we assert that a sparse representation of the refractivity field can be obtained using, e.g., a dictionary composed of Kronecker products of Discrete Cosine Transform (DCT) letters in longitude and latitude directions and of Euler letters and Dirac letters in the height direction. That is, the letters *C* illustrated in Fig. 4 correspond to DCT letters in longitude and latitude and the letters *D* and *E* correspond to Dirac letters and to Euler letters in the height direction.

In the context of neutrospheric water vapor tomography, the DCT *letters* in longitude and latitude shall represent horizontal refractivity variations, the Euler letters describe the

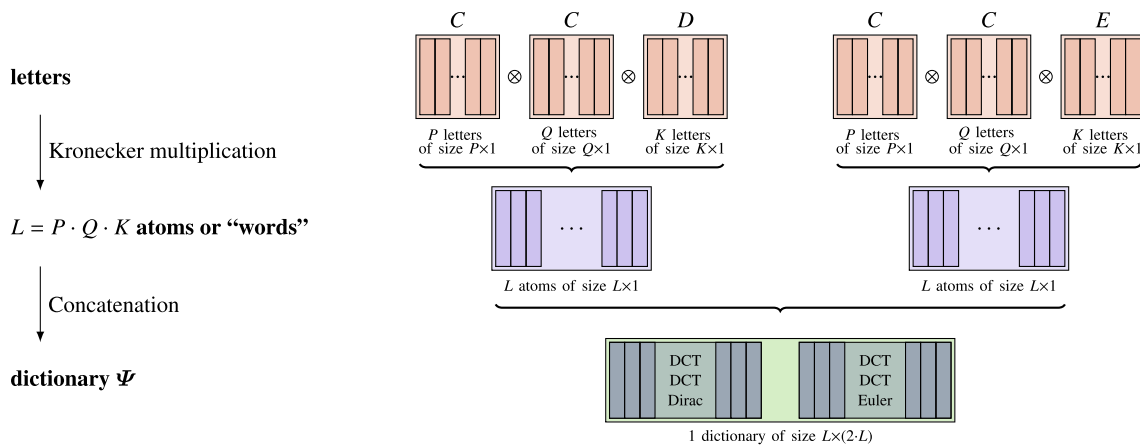


Fig. 4 Relation of *letters*, *atoms*, and *dictionaries*. An *atom* corresponds to one column of the dictionary Ψ . When referring to languages, an *atom* would correspond to a word within a dictionary. As each word within a language dictionary would be composed of different *letters*, each *atom* within the dictionary for sparse representation is obtained by Kronecker multiplication of smaller items, called *letters* in the following. The dictionary Ψ is used in order to transform the coefficients in the sparse representation to the parameters in the original domain: $x = \Psi \cdot s$.

In this study, the square C summarizes P DCT letters of size $P \times 1$ in longitude or Q letters of size $Q \times 1$ in latitude. The squares D and E summarize K Dirac letters of size $K \times 1$ and the K Euler letters of size $K \times 1$ in the height direction. In case of the DCT letters and the Dirac letters, the number of letters is consciously chosen equal to the letters' dimension in order to span the whole DCT space and the whole Dirac space. In contrast, when considering the Euler letters, the number of letters could also differ from K

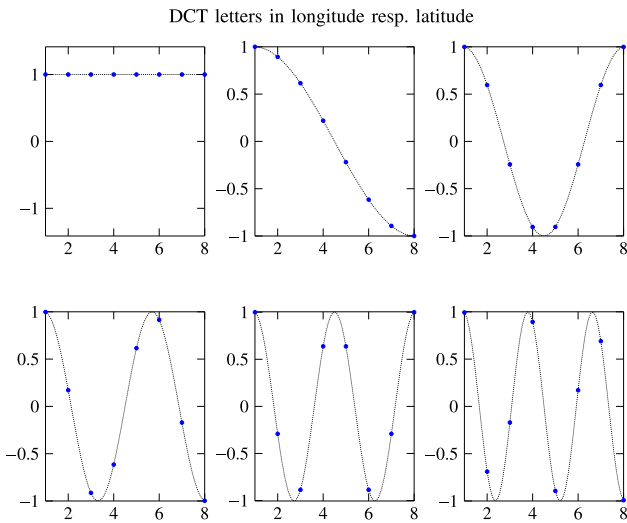


Fig. 5 Representation of six 1D Discrete Cosine Transform letters describing the neutrospheric behavior in the longitude or latitude directions. Atoms for the 3D dictionary for sparse representation can be deduced by Kronecker multiplication of the DCT letters in longitude with those in latitude and with the Euler and Dirac letters in the height direction. The black dotted lines indicate the course of the function of the DCT letters. The sampling points are highlighted in blue. The axis of abscissae shows the voxel number in longitude or in latitude

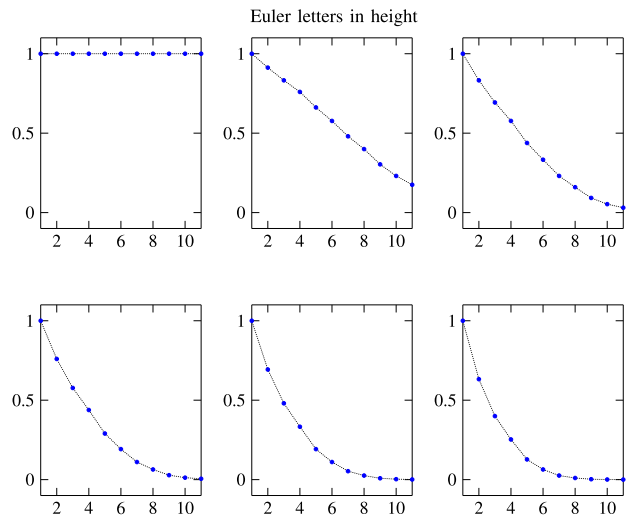


Fig. 6 Representation of six 1D Euler letters modeling the refractivity decrease with height. Atoms for the 3D dictionary for sparse representation can be deduced by Kronecker multiplication of the Euler letters in the height direction with the letters chosen for the longitude and the latitude directions. The black dotted lines indicate the course of the function. The sampling points are highlighted in blue. The axis of abscissae shows the voxel number in height

refractivity decay with height, and the Dirac letters model deviations from a decay that could exactly be described by a linear combination of Euler letters. Examples for the mentioned letters are shown in Figs. 5 and 6, and an example for atoms of a 3D dictionary is shown in Fig. 7.

According to Annadurai (2007), the inverse DCT yielding a signal $f(r_1)$ based on its transform $F(r_2)$ is defined as

$$f(r_1) = \sum_{r_2=1}^R w(r_2) \cdot \cos \left[\frac{(2 \cdot r_1 - 1) \cdot (r_2 - 1) \cdot \pi}{2 \cdot R} \right] \cdot F(r_2) \tag{42}$$

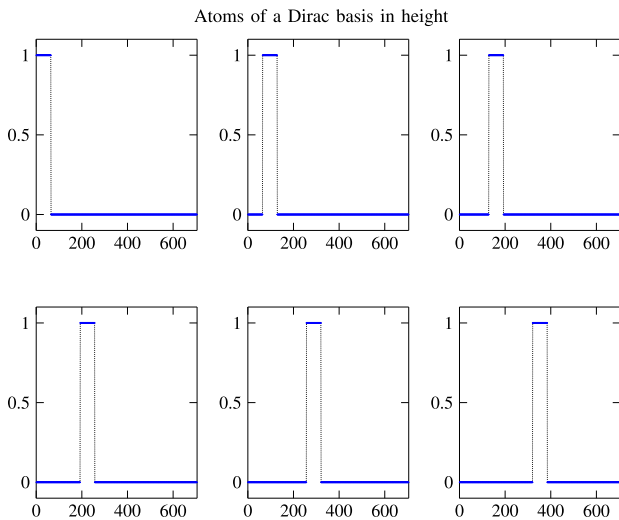


Fig. 7 Representation of six atoms of a 3D Dirac basis dictionary, which might be used in order to correct deviations from a decay with height represented by linear combinations of atoms that are based on Euler letters in the height direction. The Dirac letters in the height direction are combined with constant letters in longitude and latitude. The black dotted lines indicate the course of the function of the 3D Dirac basis. The sampling points are highlighted in blue. The axis of abscissae shows the parameter numbers $1 \dots M$ in the transform domain. The estimated solution in the transform domain corresponds to a linear combination of all atoms

with parameter indices $r_1 = 1 \dots R$ in the original domain, $r_2 = 1 \dots R$ in the transform domain, and

$$w(r_2) = \begin{cases} 1 & \text{if } r_2 = 1 \\ \frac{1}{\sqrt{R}} & \\ \frac{1}{\sqrt{\frac{2}{R}}} & \text{else.} \end{cases} \quad (43)$$

In case of the representation of a 3D water vapor signal in a sparse transform domain, the transform $F(r_2)$ is still unknown when the letters building the atoms of the transform are defined. However, a single letter only corresponds to one addend of the sum in Eq. 42 and thus is defined as

$$C(r_1, r_2) = w(r_2) \cdot \cos\left(\frac{\pi}{2 \cdot R} \cdot (2 \cdot r_1 - 1) \cdot (r_2 - 1)\right). \quad (44)$$

The r_1 1D Euler letters $E_{r_1 r_h}$ for the vertical direction are given by

$$E(r_1, r_h) = \exp\left(-\frac{r_1 \cdot (r_h - 1)}{\alpha}\right) \quad (45)$$

where the k th element of r_h ($k = 1 \dots K$) is proportional to the height of the upper border of the k th voxel layer.

Each letter can be imagined to describe the neutrospheric behavior in one of the three signal dimensions longitude,

latitude, and height. The parameter R in Eqs. 44 and 45 stands for the number of voxels in the respective dimension. The steepness of the Euler decay is represented by α . For this study, different values of α out of the reasonable interval $\alpha \in [2; 10]$ are introduced.

The Dirac atoms have compact support: they deviate from zero only in a small interval. If Dirac letters in the height direction are considered, they can, e.g., be zero for all but one height layer.

Based on many different 1D letters Ψ_{1D} for each of the three signal directions longitude, latitude, and height, a Kronecker product (\otimes) yields the corresponding 3D dictionary:

$$\Psi = \Psi_{1D,h} \otimes \Psi_{1D,l} \otimes \Psi_{1D,\lambda} \quad (46)$$

The work in Henderson and Searle (1981) defines the Kronecker product of the matrices $A \in \mathbb{R}^{s \times t}$ and $B \in \mathbb{R}^{u \times v}$ as the $su \times tv$ matrix

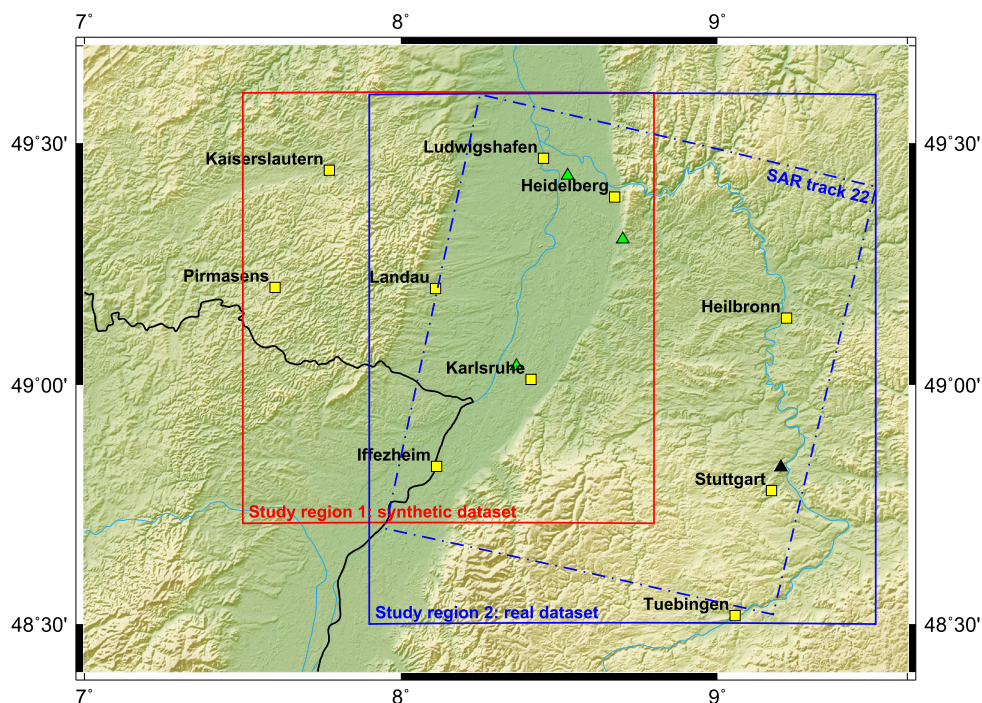
$$A \otimes B = \{a_{ij} \cdot B\}_{ij} = \begin{bmatrix} a_{11} \cdot B & a_{12} \cdot B & \dots & a_{1u} \cdot B \\ a_{21} \cdot B & a_{22} \cdot B & \dots & a_{2u} \cdot B \\ \vdots & \vdots & \ddots & \vdots \\ a_{s1} \cdot B & a_{s2} \cdot B & \dots & a_{su} \cdot B \end{bmatrix}. \quad (47)$$

Figure 7 shows atoms of a 3D dictionary obtained by Kronecker multiplication of two constant functions corresponding to letters in longitude and latitude and Dirac letters in the height direction.

Similar to the common Fourier transform, the signal representation in the original domain is obtained by building linear combinations of the atoms resp. base functions. The coefficients of s are obtained from solving Eq. 39, where the minimization of the L_1 norm in the regularization term ensures that only a small number of atoms are selected and most of the coefficients are zero. As in the LSQ case, equal weights have again been assigned to the observations, and prior knowledge from three surface meteorological sites is introduced. The trade-off parameter λ_{CS} between L_1 norm and L_2 norm term in Eq. 39 is selected in a similar way as the trade-off parameters λ_{hz} , λ_{vert} and λ_{meteo} in the LSQ case in Sect. 5.2.

However, instead of setting an eigenvalue cutoff criterion as in the LSQ case, a set of stable solutions is selected based on the sparsity of the solution. The number of sparse coefficients in the DCT Euler Dirac domain containing 99.9 % of the signal power is required to lie between 5 and 15 % of the total number M of coefficients in the transform domain, which ensures a sparse, yet not too sparse solution. Thereafter, based on the preselection above, the final trade-off parameter is again chosen by minimizing the observation residuals. As H_{scale} is crucial for the vertical constraint in the

Fig. 8 Study areas for the synthetic and the real dataset. The study area 2 (real data) contains the Envisat SAR frame of track 22 in the Upper Rhine Graben. Yellow squares indicate the available GNSS sites. The black triangle indicates the radiosonde site 10739 in Stuttgart. The surface meteorological sites yielding prior knowledge on the surface refractivity are represented by green triangles



LSQ case, the definition of an appropriate steepness parameter α is crucial for the parametrization of the vertical decay in CS. In contrast to the LSQ case, where H_{scale} is chosen during the selection of the trade-off parameters, in the case of CS, α is selected automatically by choosing appropriate atoms out of the dictionary within the minimization process.

6 Study regions and datasets

GNSS observations of seven resp. eight GNSS receivers are available within each of the two $95 \times 99 \text{ km}^2$ resp. $117 \times 122 \text{ km}^2$ large study areas in the Upper Rhine Graben (URG) in southern Germany and eastern France shown in Fig. 8. As indicated in Fuhrmann et al. (2013), the URG region is geophysically very stable, disposing of annual deformations in the order of 0.5 mm in the horizontal direction and about ± 0.2 mm in the vertical direction. Therefore, the study region is suitable for our research, in which InSAR atmospheric phases need to be distinguished from the InSAR deformation phases.

Within study region 1, GNSS observations and surface meteorological information define a real observing geometry that can be used to generate a synthetic dataset. We use 3D water vapor fields with a resolution of 900 m in longitude and in latitude from the WRF modeling system in order to produce synthetic *SWD* observations.

Within the real dataset corresponding to study region 2, GNSS *SWD* estimates of eight observing sites can be used. Moreover, InSAR neutrospheric phase maps derived from a total number of seven ASAR acquisitions of the C-band

Envisat satellite track 22 are available at a 35 days repeat cycle. The SAR acquisition time in track 22 is 9h48 UTC. A total number of 332828 PS points has been detected. Finally, radiosonde profiles at the radiosonde site 10739 in Stuttgart as well as observations of three surface meteorological sites are available for study region 2.

The study regions 1 and 2 are discretized into $7 \times 5 \times 11$ resp. $9 \times 6 \times 11$ voxels, each of a horizontal size of about $20 \text{ km} \times 20 \text{ km}$. The height layer thicknesses are set to 500, 500, 500, 500, 750, 750, 1000, 1000, 1500, 1500, and 1500 m, increasing from the surface to the higher layers.

In this study, only GPS observations are used. The cutoff elevation angle is set to $\epsilon_{\text{cut}} = 7^\circ$, and GPS observation epochs of ± 15 min around the SAR acquisition time are used. The sampling rate of the GPS observations corresponds to 30 seconds.

6.1 Synthetic dataset based on WRF

Based on the observing geometry of the available GNSS and InSAR measurements, synthetic *SWDs* are calculated from the WRF data. This enables a direct comparison of the later estimated 3D water vapor field with the reference data available from WRF.

The synthetic GNSS dataset is generated based on WRF using the azimuth and elevation angles of real GNSS rays as well as real GNSS site coordinates in longitude and latitude. The height of the sites for the synthetic dataset corresponds to the height of the WRF Digital Elevation Model (DEM) at the longitude and latitude given by the GNSS sites. The

WRF simulation output (water vapor mixing ratios, pressure, temperature) is transformed into wet refractivities as shown in Fig. 2. Thereafter, Eq. 9 and a direct raytracing along the real GNSS rays yield the synthetic GNSS $SWDs$.

For the synthetic InSAR dataset, additional sites and rays can be simulated at any point on the WRF DEM using artificial directions that emulate a possible satellite geometry, e.g., with azimuth angles A between 0° and 360° and with elevation angles ϵ between $\epsilon_{\text{cut}} = 7^\circ$ and $\epsilon_{\text{max}} = 90^\circ$. For these *synthetic InSAR sites*, the procedure generating synthetic $SWDs$ is the following. All those WRF cells of the lowest WRF layer are determined that are horizontally situated within a radius r_{average}

$$r_{\text{average}} = \frac{H_{\text{scale}}}{\tan \epsilon_{\text{cut}}} \quad (48)$$

around the considered synthetic InSAR site, where H_{scale} is set to some mean scale height for the considered study region, e.g., to 1500 m. For each of the selected WRF cells of the lowest layer, a ZWD value is then integrated along the vertical column above the cell. These $ZWDs$ for the WRF cell columns surrounding the synthetic InSAR site are averaged, and the corresponding $SWDs$ are obtained by means of mapping the cylindric average $ZWDs$ into the artificial ray directions defined above. The mapping of the $ZWDs$ to the slant direction is performed by dividing the $ZWDs$ by the sine of the respective elevation angle. No gradients are considered in the synthetic dataset. In this study, 35 synthetic InSAR sites are defined within the horizontal centers of the 7×5 ground voxels, at a height given by the WRF DEM. A total of 20 rays per site is defined.

As described in Sect. 5, the tomographic system is regularized by means of horizontal and vertical constraints as well as prior knowledge from surface meteorology. In case of the synthetic dataset, this prior knowledge is obtained from the WRF model.

A 3D validation of the reconstructed refractivities within the tomographic voxels is done using the input WRF refractivities averaged in the tomographic grid.

6.2 Real dataset based on GNSS and InSAR

In case of the real dataset, the tomographic reconstruction relies on total SWD estimates from GNSS PPP and PSI. On the one hand, GNSS SWD estimates are included into the system of equations. These $ZWDs$ are separated from the Zenith Total Delays ($ZTDs$) estimated by Bernese GNSS Software 5.0 by means of subtracting the Zenith Hydrostatic Delays ($ZHDs$) derived from the Saastamoinen model

$$ZHD^{\text{model, meteo}} = 0.002277 \cdot D_{h,\varphi} \cdot p_0. \quad (49)$$

The quantity p_0 (hPa) corresponds to the surface pressure. The variable $D_{h,\varphi}$ depends on the latitude φ and on the height h of the site at which the neutrospheric delay is computed:

$$D_{h,\varphi} = 1 + 0.0026 \cdot \cos(2 \cdot \varphi) + 0.00028 \cdot h \text{ (km)} \quad (50)$$

In addition, the complete GNSS $SWDs$ include horizontal gradients in northing ΔN and easting ΔE estimated by the Bernese GNSS Software 5.0:

$$SWD = \left(ZTD^{\text{estimate}} - ZHD^{\text{model, meteo}} \right) \cdot mf_{\text{wet}} + \Delta N \cdot \frac{\cot \epsilon}{\sin \epsilon} \cdot \cos A + \Delta E \cdot \frac{\cot \epsilon}{\sin \epsilon} \cdot \sin A, \quad (51)$$

where the mapping function

$$mf_{\text{wet}} = \frac{1}{\sin \epsilon} \quad (52)$$

is used. No observation residuals are considered. The neutrospheric model within the GNSS processing is composed of the Saastamoinen model (hydrostatic, wet), the hydrostatic and wet Niell mapping functions, and a tilting gradient model. The estimation interval of the $ZTDs$ corresponds to 15 min. Each set of total horizontal gradient parameters is estimated for 24 h.

The optimal scenario for building 3D wet refractivity fields using GNSS tomography is to have a dense GNSS network. At each GNSS site, a SWD estimate is available as input for the tomographic system. In reality, the GNSS mean inter-site distance in the considered study region is about 50 km, i.e., the site density is quite low. However, InSAR provides a dense network of PS points at which atmospheric phases are available. Consequently, while considering GNSS $SWDs$ on the one hand, on the other hand, 2D absolute ZWD maps are introduced into the tomographic system.

In general, InSAR phases are, per definition, relative measurements given as a temporal difference between two dates. Therefore, the key idea presented in Alshawaf et al. (2015b) is the understanding of the differences between GNSS and InSAR estimates of the neutrospheric delays. Based on the understanding that GNSS and InSAR show complementary features, Alshawaf et al. (2015b) developed an approach that yields the absolute wet delay at each PS point based on GNSS $SWDs$, relative InSAR atmospheric phases, and surface meteorological information.

This synergy of GNSS and InSAR solves the problem of InSAR measurements being relative and provides absolute $ZWDs$ at each InSAR PS point. Hence, in the following, the term InSAR ZWD stands for the described, absolute $ZWDs$ obtained from GNSS InSAR combination. These InSAR ZWD estimates can be aggregated to derive real wet delay input data at given points as if corresponding to GNSS

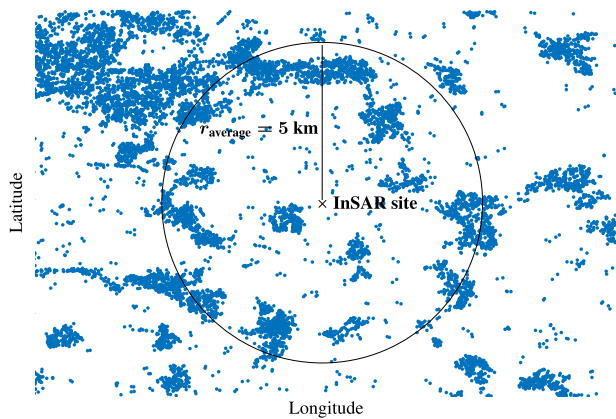


Fig. 9 Schematic illustration of the PS distribution around an InSAR site. In the figure, the $ZWDs$ of the PS points (blue dots) are averaged within a radius of 5 km (black circle) around the shown InSAR site

sites within the study area. Such InSAR $ZWDs$ can be estimated for any *InSAR site* simulated within the InSAR swath. This is done similarly to the integration of synthetic $SWDs$ based on WRF simulations in Sect. 6.1. As illustrated in Fig. 9, the InSAR $ZWDs$ of all those persistent scatterers are averaged that fall within a radius r_{average} around the defined InSAR site. That is, the InSAR $ZWDs$ are averaged around the InSAR sites, as if corresponding to averaging cylinders approximating averaging cones around each GNSS site in the GNSS observing geometry. The obtained mean ZWD values per cylinder can be mapped into artificial directions that emulate a possible satellite geometry, e.g., with azimuth angles A between 0° and 360° and elevation angles ϵ between $\epsilon_{\text{cut}} = 7^\circ$ and $\epsilon_{\text{max}} = 90^\circ$. The mapping to the slant directions is performed by dividing the $ZWDs$ by the sine of the respective elevation angle. In this study, one InSAR site is defined in the horizontal center of each voxel of the lowest tomographic layer and 20 artificial rays are defined per InSAR site. The heights of the InSAR sites are deduced from the height of the PS points situated within r_{average} around the InSAR site.

Surface meteorological information of three synoptic sites is included as prior knowledge into the tomographic system. The validation of the tomographic reconstruction using external data is only possible in Stuttgart.

7 Results

Section 7.1 gives the tomographic results for the synthetic dataset. Thereafter, Sect. 7.2 compares radiosonde and GNSS $ZWDs$ in order to get a good basis for the validation of GNSS-based resp. GNSS- and InSAR-based wet refractivities using radiosonde profiles in Sect. 7.3.

7.1 Sensitivity analysis: reconstruction quality vs. number of rays per voxel within the synthetic dataset

Within the synthetic dataset, a 3D validation of the reconstructed wet refractivity N_{wet} is possible. Analyzing the absolute value of the difference between the tomographically reconstructed refractivities and those given by WRF, Fig. 10 shows that

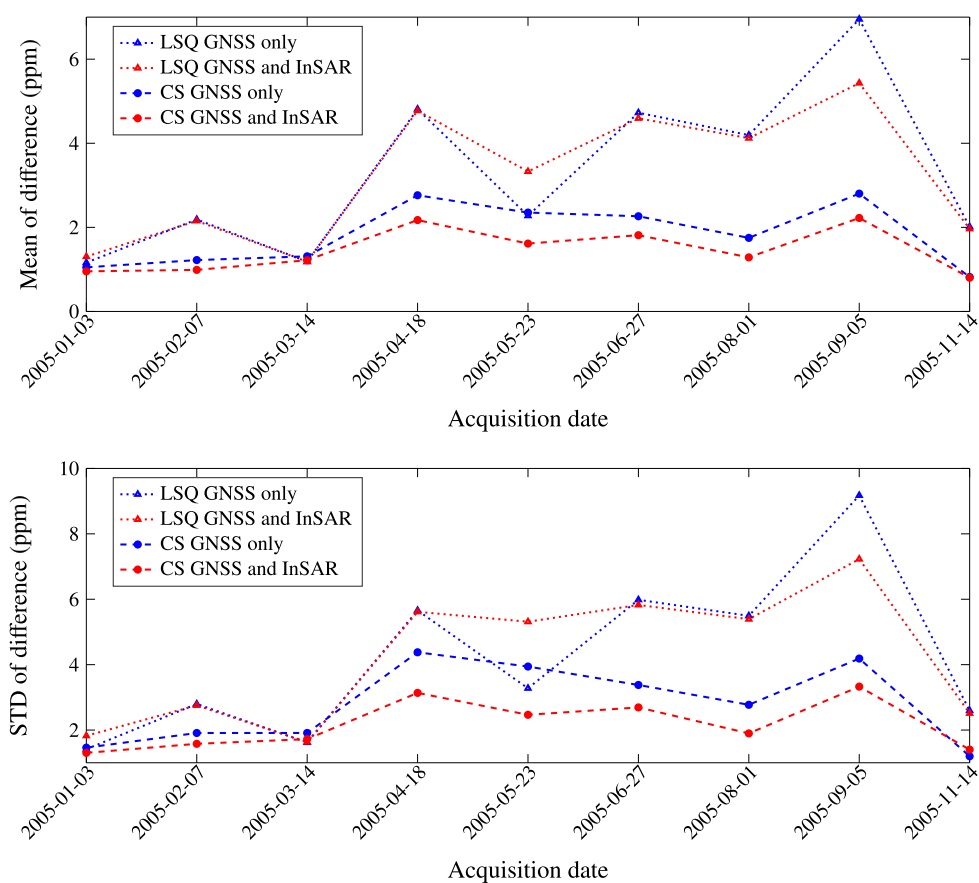
- on all but one acquisition date, both the mean and the standard deviation of the difference are smaller in case of CS than in case of LSQ,
- both the mean and the standard deviation of the difference decrease when adding InSAR into the CS solution, yet
- no clear effect of adding InSAR $SWDs$ can be observed in the case of LSQ.

When interpreting Fig. 10, the seasonal variability of water vapor has to be taken into account. In the case of increasing humidity in the summer time, i.e., in the case of larger absolute values of N_{wet} , the reconstruction quality decreases, i.e., larger values are obtained for the mean difference and the standard deviation of the difference between the WRF refractivities and the reconstructed refractivities.

For the different acquisition dates of study region 1, a total of 474 to 712 GNSS observations are available. Considering one acquisition date in more detail, a total of 712 rays are available for the seven GNSS sites available within study region 1 on 2005-01-03. Figure 11a shows how many GNSS rays are crossing the tomographic voxels on that date. Due to the cone-shaped GNSS observing geometry, most of the voxels close to the surface are crossed by much less rays than voxels in the higher tomographic layers. However, if a low voxel is crossed, the number of rays passing through it is larger than in higher atmospheric layers. On 2005-01-03, the percentage of crossed voxels increases from 20 to 94 % from the lowest to the highest layer. If synthetic InSAR observations are added, the number of crossed voxels increases, as shown in Fig. 11b. However, the absolute values of the ray numbers in Fig. 11b are smaller than those in Fig. 11a. This can be explained by the fact that in the case of GNSS, the satellite constellations of ± 15 min around the SAR acquisition time are considered, whereas in the case of InSAR only a single artificial satellite constellation is considered. Moreover, there may still remain uncrossed voxels in Fig. 11b, e.g., if an InSAR site is defined above the lowest tomographic layer or if only low elevation signals are available.

A layer-wise comparison of the estimated refractivities and the WRF refractivities for 2005-04-18 is given in Fig. 12. The refractivity differences between the tomographic reconstruction and the WRF data decrease with increasing height layers. This can be explained both by the decrease of the

Fig. 10 Upper plot: mean of the absolute difference between estimated refractivities and WRF refractivities over all voxels. Lower plot: standard deviation (STD) of the difference between estimated refractivities and WRF refractivities over all voxels. On all but one date, using CS instead of LSQ significantly improves the reconstruction accuracy and precision. Adding synthetic InSAR *SWDs* to the synthetic GNSS *SWD* only improves the solution in the case of CS



absolute value of N_{wet} with height and by the increase in rays per voxel observed in most voxels when reaching higher atmospheric layers.

The accuracy of the estimated refractivities w.r.t. the number of rays crossing the respective voxels is presented in Fig. 13. As expected, for both synthetic GNSS only and synthetic GNSS and InSAR, the refractivities within crossed voxels are more accurately and more precisely reconstructed than the refractivities within empty voxels.

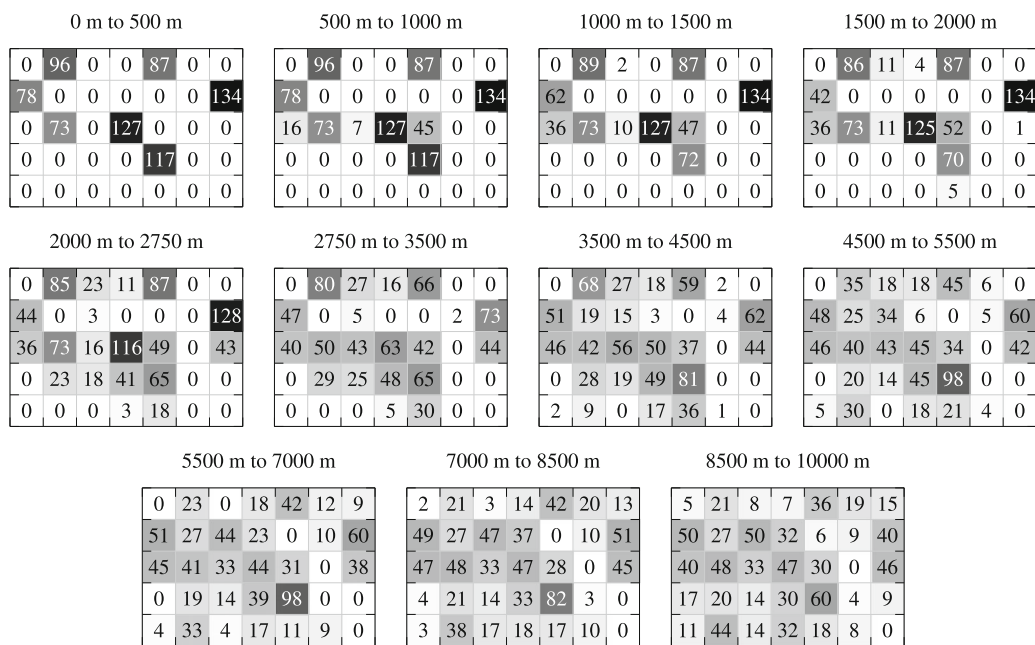
7.2 Consistency of radiosonde, GNSS, and InSAR

When aiming at a validation of a GNSS- or GNSS- and InSAR-based water vapor tomography by means of radiosonde profiles, the consistency of radiosonde and GNSS observations has to be checked. If the radiosonde humidity information and that estimated from GNSS are not consistent, a validation is not possible. Therefore, we compare the precipitable water PW measured within the whole radiosonde profiles with the PW derived from GNSS $ZWDs$. Thereafter, the quality of the GNSS and InSAR fusion yielding absolute water vapor maps is analyzed.

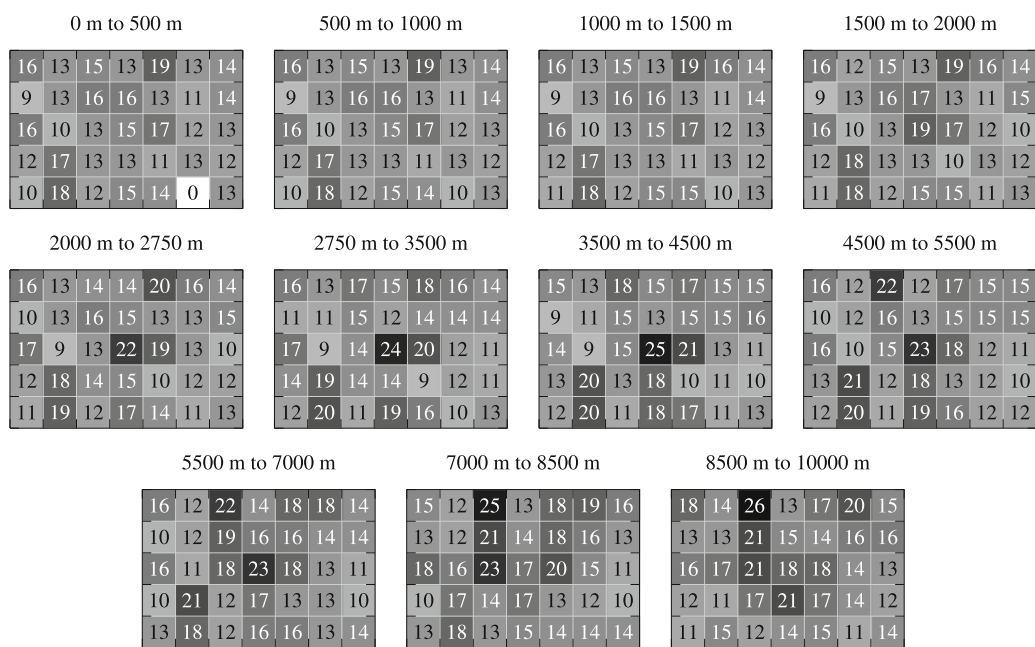
The radiosonde GNSS PW comparison is performed at 0h00 UTC and 12h00 UTC, which correspond to the start times of the available radiosonde 10739 ascents over

Stuttgart. As the distance between the Stuttgart radiosonde site and the Stuttgart GNSS site 0384 is about 6 km, the radiosonde ascent section should be covered by the GNSS geometry, even if the radiosonde does not ascend exactly vertically but is driven by winds. In addition, GNSS PW values have been computed for the SAR acquisition time at 9h48 UTC. This is done in order to get an idea of the humidity change between 0h00 UTC and 12h00 UTC.

As neutrospheric water vapor is highly variable in time and space, a validation of refractivities estimated around 9h48 UTC by means of radiosonde observations at 0h00 UTC and 12h00 UTC is not the best option. However, a linear interpolation between the two radiosonde acquisition times is an acceptable option if i) the two sensors radiosonde and GNSS match well at both 0h00 UTC and 12h00 UTC, and if ii) a linear interpolation of the GNSS PW values at 0h00 UTC and 12h00 UTC is close to the GNSS PW value observed at 9h48 UTC. In this context, we speak of a good matching and close PW values, if the PW differences between GNSS and the radiosonde are smaller than 2 mm PW at the three considered times of day. As shown in Fig. 14, this is the case on 2005-01-19, 2005-07-13, 2005-10-26, 2006-03-15, and 2006-05-24 at the radiosonde site 10739 in Stuttgart. The accepted value of 2 mm PW difference is selected based on other studies comparing radiosonde and GNSS PW . The



(a) Number of synthetic GNSS rays per voxel



(b) Number of synthetic InSAR rays per voxel

Fig. 11 Number of rays crossing the tomographic voxels on 2005-01-03 within the synthetic dataset. **a** The number of rays in the synthetic GNSS only observing geometry. **b** The number of additional rays from the synthetic InSAR observing geometry. The 5 × 7 voxels per height layer correspond to the 5 voxels in latitude and to the 7 voxels in longitude. Longitude increases along the abscissae, latitude along the ordinate. Above the plots, the heights of the layers are given. The number of rays crossing a voxel is represented by the color of the voxel. Dark voxels correspond to voxels that are crossed by many rays, white voxels are not crossed by any ray. The higher a layer is situated within the tomographic grid in **a**, the more voxels per layer are crossed. Many of the voxels in

the lowest layers are not crossed by any ray. However, if a low voxel is crossed, then the number of rays passing through it is larger than in higher atmospheric layers. The absolute values of the ray numbers of **(b)** is smaller than in the crossed ground voxels in **(a)**. This is due to the fact that in the case of synthetic GNSS, the satellite constellations of ±15 min around the SAR acquisition time are considered, whereas in the case of synthetic InSAR, only a single time stamp of artificially defined rays is considered. If due to topography synthetic InSAR sites are defined above the ground voxel, there remain voxels without any crossing rays. In this study, 20 synthetic rays are defined for each of the 35 synthetic InSAR sites

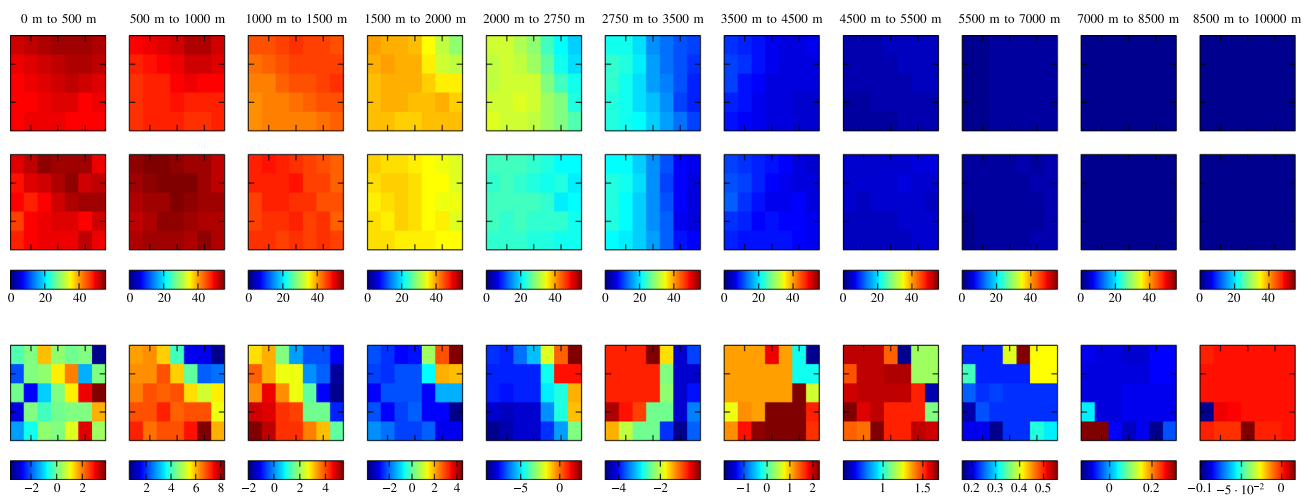
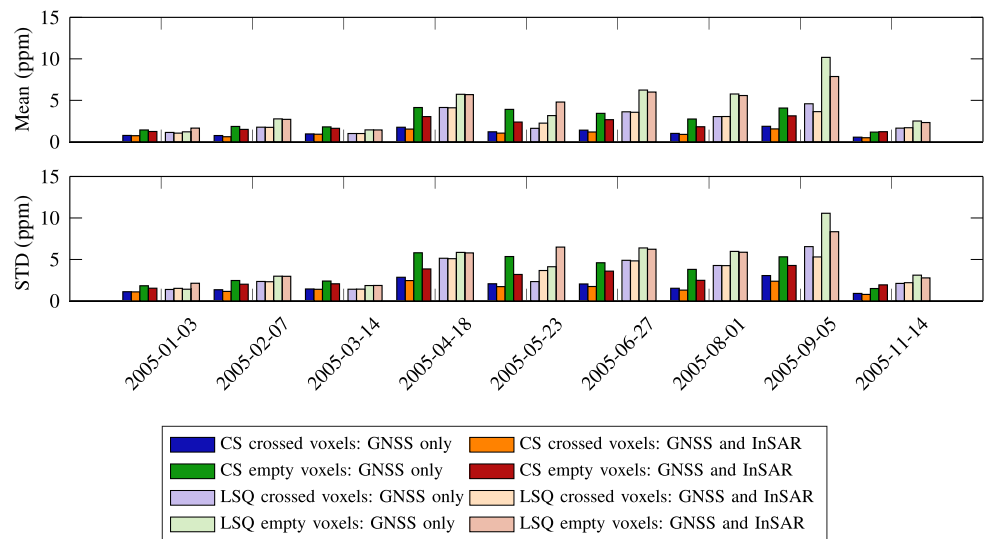


Fig. 12 Plot of 2005-04-18 layer-wise WRF refractivities, estimated refractivities from CS, and the differences between the estimation and the WRF refractivities in ppm. The 5×7 voxels per height layer correspond to the 5 voxels in latitude and to the 7 voxels in longitude.

Longitude increases along the abscissae, latitude along the ordinate. Above the plots, the heights of the layers are given. The estimates are deduced from synthetic GNSS and InSAR *SWDs*

Fig. 13 Comparison of the reconstruction accuracy within crossed voxels and voxels that are not crossed by any rays. The absolute mean value and the STD of the differences between estimated and WRF refractivities are shown for the different acquisition dates



studies in Bock et al. (2005) and Niell et al. (2001) obtained mean *PW* differences between the two sensors of 1 to 2 mm, Bock et al. (2007) even 3 mm or more.

The low temporal resolution as well as the unassured consistency of GNSS and radiosonde observations already indicate some weaknesses of a radiosonde validation. In addition, in reality, the radiosonde ascent takes some time, whereas the validation for this work assumes the radiosonde to take all the measures along the profile within a time instant.

Moreover, when introducing both GNSS and InSAR into the tomographic system, the absolute *ZWD* maps from InSAR must match well with the GNSS *ZWDs*. Therefore, the InSAR *ZWDs* of all PS points situated within $r_{average}$ around the available GNSS sites are averaged and compared

with the respective GNSS *ZWDs*. If the mean difference of GNSS and InSAR *ZWDs* is less than 10 mm over all GNSS sites per acquisition date, i.e., less than $2 \cdot \sigma_y$, the InSAR *ZWDs* are introduced into the tomographic system. In this study, this is the case for all acquisition dates except 2005-07-13 and 2006-06-28.

All in all, considering both the consistency of radiosonde and GNSS as well as that of GNSS and InSAR, the acquisition dates 2005-01-19, 2005-10-26, 2005-03-15, and 2006-05-24 remain for validation. Within these dates, the most resp. the fewest water vapor resides in the atmosphere on 2005-10-26 resp. on 2006-03-15. Therefore, these two dates representing different atmospheric states are selected for the radiosonde validation in Sect. 7.3.

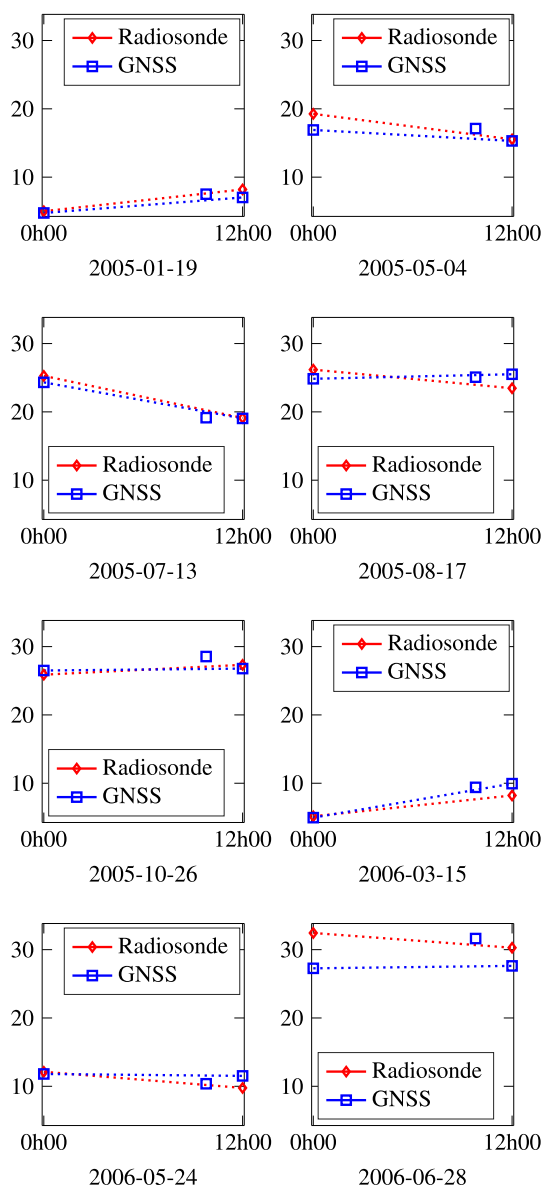


Fig. 14 Precipitable water (mm) from GNSS and radiosonde at the SAR acquisition dates of track 22. The radiosonde PW values at 0h00 UTC and 12h00 UTC correspond to radiosonde ascents starting at these times above the Stuttgart radiosonde site 10739. In the case of GNSS, the PW values are deduced from GNSS ZWD estimates of 0h00 UTC, 9h48 UTC, and 12h00 UTC. The dotted lines indicate linear interpolations between the sampling points at 0h00 UTC and 12h00 UTC

7.3 Validation of GNSS- and InSAR-based wet refractivities using radiosonde profiles

For the acquisition dates 2005-10-26 and 2006-03-15, Fig. 15 shows the agreement between the wet refractivities reconstructed by means of LSQ or CS and the radiosonde profiles. The accuracy of the tomographic results is similar for LSQ and CS. For both LSQ and CS, the deviations of the tomographic solution from the Euler decay resp. from the linear

combination of atoms based on Euler letters and Dirac letters in the height direction are not represented by the reconstructed refractivities. The height resp. the refractivity in Fig. 15 are consciously plotted on the abscisse resp. on the ordinate, in order to make the Euler refractivity decay with height visibly similar to the Euler letters used in the height direction. As the radiosonde observations correspond, both temporally and locally, to other atmospheric snapshots than the GNSS- and InSAR-based tomographic results, no quantitative comparisons are drawn. No prior knowledge of the surface meteorological site Stuttgart is included into the solution of the tomographic system.

8 Discussion and outlook

The presented research has shown that CS is a valuable method for tomographic water vapor reconstructions based on SWD observations. In the case of synthetic data, CS yields more accurate and more precise results than LSQ. When considering the GNSS only solution in average over all acquisition dates and all voxels, using CS instead of LSQ decreases the mean resp. the standard deviation of the absolute differences between estimated refractivities and WRF refractivities by about 1.5 ppm in mean resp. by about 1.4 ppm in standard deviation. In the case of the GNSS and InSAR solution, the respective values are even slightly larger, with a decrease of about 1.8 ppm in mean resp. by about 2.1 ppm in standard deviation.

In the case of CS, adding synthetic InSAR $SWDs$ slightly improves the reconstruction quality for all acquisition dates. The mean improvement over all voxels and all dates is nearly 1 ppm. In contrast, adding synthetic InSAR $SWDs$ to the LSQ solution does not show any clear effect. In general, for both LSQ and CS, voxels that are crossed by many rays are reconstructed more accurately and more precisely than voxels that are crossed by less rays. In the case of real data, no preference can be given to any solution strategy. The LSQ and the CS tomography solutions are widely consistent for both GNSS only and for GNSS and InSAR.

When comparing the LSQ and the CS solutions, we can state that in the case of LSQ, there is a risk of over-smoothing the solution by applying geometric constraints that might not be able to represent the true atmospheric behavior. Similarly, CS can only represent linear combinations of the introduced atoms, which implies that the CS solution is, for example, not very adaptive to refractivity variations in height that differ from the Euler and Dirac letters introduced in the height direction. Depending on the dictionary, there might be atmospheric behaviors that cannot be well represented by the CS atoms. However, as many different Euler letters with varying steepness are introduced in the height direction and as linear combinations of the resulting atoms can be built, the CS solu-

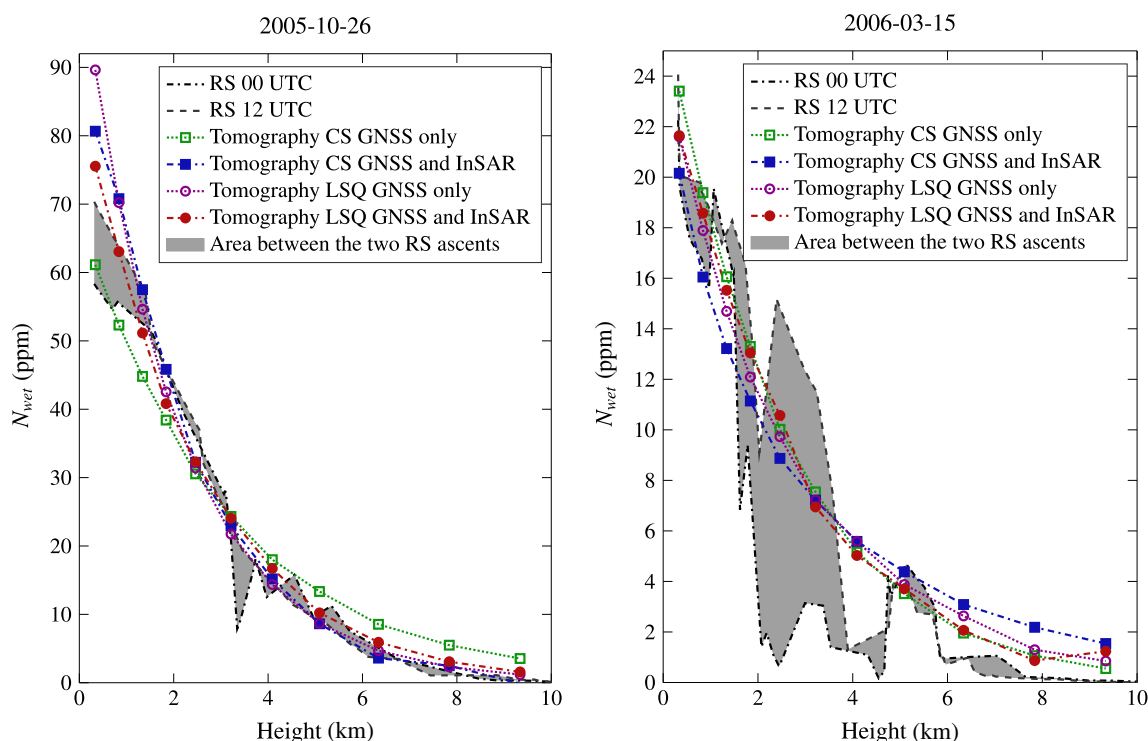


Fig. 15 Wet refractivity (ppm) on 2005-10-26 and 2006-03-15. The tomographic refractivity estimates are based on GNSS *SWDs* only resp. on GNSS and InSAR *SWDs*. The tomography solution corresponds to

9h48 UTC. The temporal window of GNSS *SWDs* introduced into the tomographic system is set to 15 min

tion should be more adaptive than the LSQ solution. More or better atoms are still necessary for further improvement of the CS solution. When local disturbances are to be reconstructed, i.e., if the refractivity is much higher in a small area of, e.g., one or two voxels, the DCT letters in longitude and latitude may not be the best option. This is due to the fact that different DCT letters may have to cancel each other in the atmospheric sections around the disturbance. However, in order to cancel out some atoms in some parts of the study region, but not in others, the total number of atoms with nonzero coefficients must be high. This, in turn, is not favored at all by the CS solution algorithm.

The balance between a potential accuracy improvement induced by a larger variety of atoms and the cost of these additional atoms in terms of sparsity of the solution should always be kept in mind. Since the CS solution requires a sparse representation of the parameters in the transform domain, selecting a high number of atoms is not possible. As in LSQ, there is a risk of over-constraining the solution. The challenge of accurately representing local atmospheric disturbances and keeping the solution sparse at the same time, might be met by introducing compactly supported letters in longitude and latitude, e.g., wavelets, instead of DCT atoms only.

In addition, the scaling of the atoms is essential for an accurate solution. We do not seek a very sparse solution with

only a single, very high coefficient corresponding to one of the decreasing Euler atoms, but we are interested in a linear combination of, e.g., 5 to 15 % of the atoms, generating a more accurate solution than a single atom could produce. This is only possible if the scaling of the most prominent Euler atoms is reasonable.

For both LSQ and CS, a good tuning of the trade-off parameters is essential. In both methodologies, a two-step trade-off parameter selection is implemented that ensures both the stability of the solution and small observation residuals. If the trade-off parameters are selected inappropriately, both LSQ and CS are incapable to produce an accurate solution. Similarly, the selection of appropriate values for the scale height H_{scale} resp. for the parameter α defining the steepness of the Euler letters is essential in the LSQ resp. CS solution.

As stated in Sect. 7.2, the validation of the tomographic solution in the real dataset is challenging: There is only one radiosonde profile available, i.e., no 3D validation is possible, but just a validation along a single profile. There might be solutions matching well along this profile, but having a bad reconstruction accuracy in the remaining parts of the study region. Furthermore, there are only radiosonde profiles available around 0 UTC and 12 UTC. As the temporal resolution of 12 h is low and as the atmospheric water

vapor is highly variable in time, no interpolation of the radiosonde data at 9h48 UTC is performed. Finally, although the radiosonde moves horizontally during its ascent, we suppose the whole profile to be situated vertically above the radiosonde site, which might cause inaccuracies in the validation. A 3D validation w.r.t. a numerical weather model could be a good alternative to the radiosonde validation. Alternatively, if temporal variations in the refractivity are included into the tomographic model, the GNSS and InSAR solution could be temporally propagated until the radiosonde ascent time. Thus, the radiosonde observations could be used in order to validate the inclusion of InSAR data into the tomographic system even though the acquisition times of InSAR and of the radiosonde differ. In the future, the potential of CS shall be investigated based on a GNSS only solution for a study region disposing of up to five radiosonde site. In order to avoid temporal interpolations, the validation will then be performed at a radiosonde acquisition time, which is, due to the InSAR data with fix acquisition time, not possible in this study.

According to Champollion et al. (2005), the optimal horizontal voxel size for GNSS-based water vapor tomography should correspond to the mean GNSS inter-site distance. In this study, the mean inter-site distance is about 50 km, and the voxel size is therefore much too small. However, if larger voxels, e.g., $2 \times 2 \times 11$ voxels of a horizontal size of about $50 \times 50 \text{ km}^2$, are defined, the spatially highly variable refractivity would be averaged over too large areas. Moreover, no sparse solution would be possible anymore, because the total number of voxels would be too small. However, as CS is capable to recover sparse signals using only a small number of measurements, even smaller voxels than in this study shall be tested in the future.

Finally, the integration of synthetic absolute GNSS and InSAR *SWDs* into the tomographic system might be improved. The GNSS and InSAR observing geometries differ, and therefore, the two measurement techniques observe different sections of the atmosphere. The horizontal resolution of InSAR atmospheric phase maps is much higher than the point-wise GNSS *ZWD* resolution. Reversely, each of the atmospheric phases at a persistent scatterer contains information on a much smaller atmospheric section than a GNSS *ZWD* averaging the atmospheric behavior within a large cone above the respective GNSS site. The mapping of such GNSS *ZWDs* into different ray directions as well as the mapping of InSAR *ZWDs* into different azimuth and elevation angles has to be further investigated. In this context, particular focus should be set on the choice of the mapping function and on a mapping of the InSAR *ZWDs* into appropriate slant directions. The mapping into uniformly distributed directions with elevation angles between 7° and 90° and with azimuth angles between 0° and 360° may cause unrealistic InSAR *SWDs* corrupting the tomographic solution, especially in

the case of significant horizontal variations in the wet refractivity. Moreover, the simple $\sin \epsilon$ mapping should be avoided, especially in the case of low elevation rays within the voxels limited by elliptical upper and lower boundaries. Therefore, in future studies, we will use more complex mapping functions depending, e.g., on the day of year, on meteorological parameters, and on the height of the considered site.

As an alternative to the proposed approach, InSAR and GNSS could also be introduced as independent inputs into the tomographic system. However, the tomographic system would then have to be solved for more unknowns and the differences between the GNSS and the InSAR observing geometries would have to be understood exactly. As the complete *SWD* product resulting from the GNSS and InSAR combination is used in this study, the observing geometries of the two systems are combined. This proceeding does not necessarily imply a loss of information. Instead, this synergy highly densified the available *ZWD* network. The *ZWD* resp. *PW* product generated by combining InSAR and GNSS was validated and proved to show strong correlation with other datasets. Alshawaf et al. (2015b) compared the derived *PW* maps with *PW* maps measured by the optical sensor MEdium-Resolution Imaging Spectrometer. The results of Alshawaf et al. (2015b) show strong spatial correlation between the two datasets, with values of uncertainty of less than 1.5 mm.

In future work, the potential of including observations of two SAR satellites with different viewing angles, e.g., in descending and in ascending mode, shall be analyzed.

Acknowledgements The first author was supported by a scholarship of the Deutsche Telekom Stiftung. Thanks to Franz Ulmer for providing WRF data. The work of X. Zhu is jointly supported by the European Research Council (ERC) under the European Unions Horizon 2020 research and innovation programme (Grant agreement No [ERC-2016-StG-714087], Acronym: So2Sat), Helmholtz Association under the framework of the Young Investigators Group “SIPEO” (VH-NG-1018, www.sipeo.bgu.tum.de)

Open Access This article is distributed under the terms of the Creative Commons Attribution 4.0 International License (<http://creativecommons.org/licenses/by/4.0/>), which permits unrestricted use, distribution, and reproduction in any medium, provided you give appropriate credit to the original author(s) and the source, provide a link to the Creative Commons license, and indicate if changes were made.

References

- Aguilera E, Nannini M, Reigber A (2013) A data-adaptive compressed sensing approach to polarimetric SAR tomography of forested areas. *IEEE Geosci Remote Sens Lett* 10(3):543–547
- Alonso MT, López-Dekker P, Mallorquí JJ (2010) A novel strategy for radar imaging based on compressive sensing. *IEEE Trans Geosci Remote Sens* 48(12):4285–4295
- Alshawaf F, Fersch B, Hinz S, Kunstmann H, Mayer M, Meyer F (2015a) Water vapor mapping by fusing InSAR and GNSS remote

- sensing data and atmospheric simulations. *Hydrol Earth Syst Sci* 19(12):4747–4764
- Alshawaf F, Hinz S, Mayer M, Meyer F (2015b) Constructing accurate maps of atmospheric water vapor by combining interferometric synthetic aperture radar and GNSS observations. *J Geophys Res Atmos* 120:1391–1403
- Annadurai S (2007) *Fundamentals of digital image processing*. Pearson Education, New Delhi
- Baraniuk R, Davenport MA, Duarte MF, Hegde C (2014) An introduction to compressive sensing. OpenStax CNX 27.08.2014. <http://cnx.org/contents/f70b6ba0-b9f0-460f-8828-e8fc6179e65f@5.12>
- Bender M, Dick G, Ge M, Deng Z, Wickert J, Kahle HG, Raabe A, Tetzlaff G (2011) Development of a GNSS water vapour tomography system using algebraic reconstruction techniques. *Adv Space Res* 47(10):1704–1720
- Benevides P, Nico G, Catalão J, Miranda P (2016) Bridging InSAR and GPS tomography: a new differential geometrical constraint. *IEEE Trans Geosci Remote Sens* 54(2):697–702
- Berger M, Moreno J, Johannessen JA, Levelt PF, Hanssen RF (2012) ESA's sentinel missions in support of Earth system science. *Remote Sens Environ* 120:84–90
- Bevis M, Businger S, Herring TA, Rocken C, Anthes RA, Ware RH (1992) GPS meteorology: remote sensing of atmospheric water vapor using the global positioning system. *J Geophys Res Atmos* 97(D14):15,787–15,801
- Bieniarz J, Aguilera E, Zhu XX, Müller R, Reinartz P (2015) Joint sparsity model for multilook hyperspectral image unmixing. *IEEE Geosci Remote Sens Lett* 12(4):696–700
- Bock O, Keil C, Richard E, Flamant C, Mn Bouin (2005) Validation of precipitable water from ECMWF model analyses with GPS and radiosonde data during the MAP SOP. *Q J R Meteorol Soc* 131(612):3013–3036
- Bock O, Bouin MN, Walpersdorf A, Lafore JP, Janicot S, Guichard F, Agusti-Panareda A (2007) Comparison of ground-based GPS precipitable water vapour to independent observations and NWP model reanalyses over Africa. *Q J R Meteorol Soc* 133(629):2011–2027
- Budillon A, Evangelista A, Schirizzi G (2011) Three-dimensional SAR focusing from multipass signals using compressive sampling. *IEEE Trans Geosci Remote Sens* 49(1):488–499
- Candès EJ, Wakin MB (2008) An introduction to compressive sampling. *Signal Process Mag IEEE* 25(2):21–30
- Champollion C, Masson F, Van Baelen J, Walpersdorf A, Chry J, Doerflinger E (2004) GPS monitoring of the tropospheric water vapor distribution and variation during the 9 September 2002 torrential precipitation episode in the Cévennes (southern France). *J Geophys Res Atmos*
- Champollion C, Masson F, Bouin MN, Walpersdorf A, Doerflinger E, Bock O, Van Baelen J (2005) GPS water vapour tomography: preliminary results from the ESCOMPTE field experiment. *Atmos Res* 74(1):253–274
- Chen B, Liu Z (2016) Assessing the performance of troposphere tomographic modeling using multi-source water vapor data during Hong Kong's rainy season from May to October 2013. *Atmos Meas Tech Discuss* 2016:1–23
- Davis J, Herring T, Shapiro I, Rogers A, Elgered G (1985) Geodesy by radio interferometry: effects of atmospheric modeling errors on estimates of baseline length. *Radio Sci* 20(6):1593–1607
- Davis JL, Elgered G, Niell AE, Kuehn CE (1993) Ground-based measurement of gradients in the “wet” radio refractivity of air. *Radio Sci* 28(06):1003–1018
- Elosegui P, Ruis A, Davis J, Ruffini G, Keihm S, Brki B, Kruse L (1998) An experiment for estimation of the spatial and temporal variations of water vapor using GPS data. *Phys Chem Earth* 23(1):125–130
- Flores A, Ruffini G, Rius A (2000) 4D tropospheric tomography using GPS slant wet delays. *Ann Geophys Springer* 18:223–234
- Fuhrmann T, Heck B, Knipfler A, Masson F, Mayer M, Ulrich P, Westerschhaus M, Zippelt K (2013) Recent surface displacements in the Upper Rhine Graben — preliminary results from geodetic networks. *Tectonophysics* 602:300–315
- Gradinarsky LP, Jarlemark P (2004) Ground-based GPS tomography of water vapor: analysis of simulated and real data. *J Meteorol Soc Jpn* 82(1B):551–560
- Grohnfeldt C, Zhu XX, Bamler R (2013) Jointly sparse fusion of hyperspectral and multispectral imagery. In: 2013 IEEE international geoscience and remote sensing symposium (IGARSS), pp 4090–4093
- Hajj GA, Ibaez-Meier R, Kursinski ER, Romans LJ (1994) Imaging the ionosphere with the global positioning system. *Int J Imaging Syst Technol* 5(2):174–187
- Hanssen R (2001) *Radar interferometry. Remote sensing and digital image processing*, vol 2. Kluwer Academic Publishers, Dordrecht
- Henderson HV, Searle SR (1981) The vec-permutation matrix, the vec operator and Kronecker products: a review. *Linear Multilinear Algebra* 9(4):271–288
- Heublein M, Zhu XX, Alshawaf F, Mayer M, Bamler R, Hinz S (2015) Compressive sensing for neutrospheric water vapor tomography using GNSS and InSAR observations. In: 2015 IEEE international geoscience and remote sensing symposium (IGARSS), pp 5268–5271
- Hirahara K (2000) Local GPS tropospheric tomography. *Earth Planets Space* 52(11):935–939
- Hooper A, Segall P, Zebker H (2007) Persistent scatterer interferometric synthetic aperture radar for crustal deformation analysis, with application to Volcán Alcedo, Galápagos. *J Geophys Res* 112:B07407
- Iordache MD, Bioucas-Dias JM, Plaza A (2011) Sparse unmixing of hyperspectral data. *IEEE Trans Geosci Remote Sens* 49(6):2014–2039
- Jiang C, Zhang H, Shen H, Zhang L (2014) Two-step sparse coding for the pan-sharpening of remote sensing images. *IEEE J Sel Top Appl Earth Obs Remote Sens* 7(5):1792–1805
- Kouba J, Héroux P (2001) Precise point positioning using IGS orbit and clock products. *GPS Solut* 5(2):12–28
- Li S, Yang B (2011) A new pan-sharpening method using a compressed sensing technique. *IEEE Trans Geosci Remote Sens* 49(2):738–746
- Niell A, Coster A, Solheim F, Mendes V, Toor P, Langley R, Upham C (2001) Comparison of measurements of atmospheric wet delay by radiosonde, water vapor radiometer, GPS, and VLBI. *J Atmos Ocean Technol* 18(6):830–850
- Notarpietro R, Gabella M, Perona G (2008) Tomographic reconstruction of neutral atmospheres using slant and horizontal wet delays achievable through the processing of signal observed from small GPS networks. *Ital J Remote Sens* 40(2):63–74
- Parker AL (2017) Systematic assessment of atmospheric uncertainties for InSAR data at volcanic arcs using large-scale atmospheric models: Application to the Cascade Volcanoes. Springer, pp 59–90
- Perler D (2011) Water vapor tomography using global navigation satellite systems. Ph.D. thesis, ETH Zürich, Nr. 20012
- Petit G, Luzum B (2010) IERS conventions. Technical report, Bureau international des poids et mesures Sevres (France)
- Potter LC, Ertin E, Parker JT, Cetin M (2010) Sparsity and compressed sensing in radar imaging. *Proc IEEE* 98(6):1006–1020
- Pruente L (2010) Application of compressed sensing to SAR/GMTI-data. In: 8th European Conference on Synthetic Aperture Radar (EUSAR), VDE, pp 1–4
- Rohm W (2013) The ground GNSS tomography-unconstrained approach. *Adv Space Res* 51(3):501–513

- Schüler T (2001) On ground-based GPS tropospheric delay estimation. Bundeswehr University Munich
- Smith EK, Weintraub S (1953) The constants in the equation for atmospheric refractive index at radio frequencies. *Proc IRE* 41(8):1035–1037
- Song S, Zhu W, Ding J, Peng J (2006) 3D water-vapor tomography with Shanghai GPS network to improve forecasted moisture field. *Chin Sci Bull* 51(5):607–614
- Stull R (2016) Practical meteorology: An algebra-based survey of atmospheric science. BC Campus
- Tang W, Liao M, Yuan P (2016) Atmospheric correction in time-series SAR interferometry for land surface deformation mapping — A case study of Taiyuan, China. *Adv Space Res* 58(3):310–325
- Troller M, Geiger A, Brockmann E, Bettems JM, Bürki B, Kahle HG (2006) Tomographic determination of the spatial distribution of water vapor using GPS observations. *Adv Space Res* 37(12):2211–2217
- Wiggins RA (1972) The general linear inverse problem: implication of surface waves and free oscillations for Earth structure. *Rev Geophys* 10(1):251–285
- Xia P, Cai C, Liu Z (2013) GNSS troposphere tomography based on two-step reconstructions using GPS observations and COSMIC profiles. *Ann Geophys Copernic GmbH* 31:1805–1815
- Yao Y, Zhao Q (2016) Maximally using GPS observation for water vapor tomography. *IEEE Trans Geosci Remote Sens* 54(12):7185
- Yao Y, Zhao Q (2017) A novel, optimized approach of voxel division for water vapor tomography. *Meteorol Atmos Phys* 129(1):57–70
- Zhang B, Hong W, Wu Y (2012) Sparse microwave imaging: principles and applications. *Sci China Inf Sci* 55(8):1722–1754
- Zhang L, Xing M, Qiu CW, Li J, Sheng J, Li Y, Bao Z (2010) Resolution enhancement for inversed synthetic aperture radar imaging under low SNR via improved compressive sensing. *IEEE Trans Geosci Remote Sens* 48(10):3824–3838
- Zhu XX, Bamler R (2010) Tomographic SAR inversion by L_1 -norm regularization — The compressive sensing approach. *IEEE Trans Geosci Remote Sens* 48(10):3839–3846
- Zhu XX, Bamler R (2013) A sparse image fusion algorithm with application to pan-sharpening. *IEEE Trans Geosci Remote Sens* 51(5):2827–2836
- Zhu XX, Bamler R (2014) Superresolving SAR tomography for multidimensional imaging of urban areas: compressive sensing-based TomoSAR inversion. *IEEE Signal Process Mag* 31(4):51–58
- Zhu XX, Bamler R (2015) Exploiting sparsity in remote sensing and earth observation: theory, applications and future trends. In: 2015 IEEE international geoscience and remote sensing symposium (IGARSS), pp 2840–2843. IEEE
- Zhu XX, Grohnfeldt C, Bamler R (2016) Exploiting joint sparsity for pansharpening: the J-SparseFI algorithm. *IEEE Trans Geosci Remote Sens* 54(5):2664–2681